INVITED PAPER

Lattice Resonances in Optical Metasurfaces With Gain and Loss

By Radoslaw Kolkowski and A. Femius Koenderink

ABSTRACT | Periodic lattices of strongly scattering objects coupled to active media are of central importance in applied nanophotonics, serving as light-emitting metasurfaces of tailored emission properties and promising an attractive platform for testing novel physical concepts and realization of unprecedented light-shaping functions. We provide an overview of the semianalytical Green function method with Ewald lattice summation applied to the investigation of surface lattice resonances in periodic arrays of resonant nanoscatterers with gain and loss. This theory is meant as a minimal model for plasmonic lattices and metasurfaces with gain: minimal in complexity, yet sufficiently rich to be a self-consistent, fully retarded multiple scattering model. It enables to include the electromagnetic interactions between electric and/or magnetic point dipoles of arbitrary orientation and arrangement, taking into account retardation and tensorial nature of these interactions and including radiation damping. It gives access to the far-field observables (reflection/transmission), as well as to the photonic band structure of guided modes. At the same time, it does not violate the optical theorem, as opposed to the commonly used tight-binding or quasi-static models. After extending the lattice Green function formalism to include gain and loss in the unit cell, we demonstrate the effects of parity-time (PT) symmetry breaking in active-lossy plasmonic arrays: the emergence of exceptional points, nontrivial topology of photonic bands, diverging effective unit-cell polarizability, and spin polarization in the PT-broken phase.

KEYWORDS | Exceptional points (EPs); parity-time (PT) symmetry; plasmonic nanoparticle arrays; non-Hermitian photonics

AQ:1 Manuscript received July 9, 2019; revised September 1, 2019; accepted September 1, 2019. *(Corresponding author: A. Femius Koenderink.)*
The authors are with the Center for Nanophotonics, AMOLF, 1098 XG Amsterdam, The Netherlands (e-mail: f.koenderink@amolf.nl).

Digital Object Identifier 10.1109/JPROC.2019.2939396

I. INTRODUCTION

The purpose of this section is to briefly review recent state of the art in the field of optical metasurfaces based on plasmonic arrays. It makes the tutorial part of this article, together with Sections II and III, which provide a didactic self-consistent description of the theory of light scattering by periodic resonant nanoparticle arrays with gain and loss. Readers interested in new research results can find them in Section IV, followed by the outlook in Section V.

The physics of periodic 2-D arrays of very strongly scattering resonant subwavelength building blocks is a cornerstone of research in active nanophotonics, appearing in various guises throughout the disciplines of plasmonics [1]–[3], metasurface science [4], [5], and the emerging field of topological and non-Hermitian photonics [6], [7]. Plasmonics traditionally focuses on exploiting the collective excitation of free electrons in noble metals for enhanced coupling of light to matter. Notably, plasmon oscillations in nanoparticles are associated with substantial and localized field enhancement. However, as plasmon excitations in single nanoparticles, often dubbed "nanoantennas," have intrinsically low quality factor due to radiative and absorptive damping, there has been a lot of interest in diffractive nanoparticle arrays. As first noted by Zou *et al.* [8], the limitations on quality factor can be largely removed by coupling nanoantennas in diffractive arrays via hybridization of the localized plasmon resonances with grating anomalies [Fig. 1(a)]. The resulting "surface lattice resonances" or "waveguide-plasmon polaritons" have enabled a variety of active nanophotonic applications [1], [2]. Notably, these include record efficiency structures for enhancing the brightness and directivity of ensembles of fluorophores [Fig. 1(b)], a holy grail for solid-state lighting phosphors [9], [10].

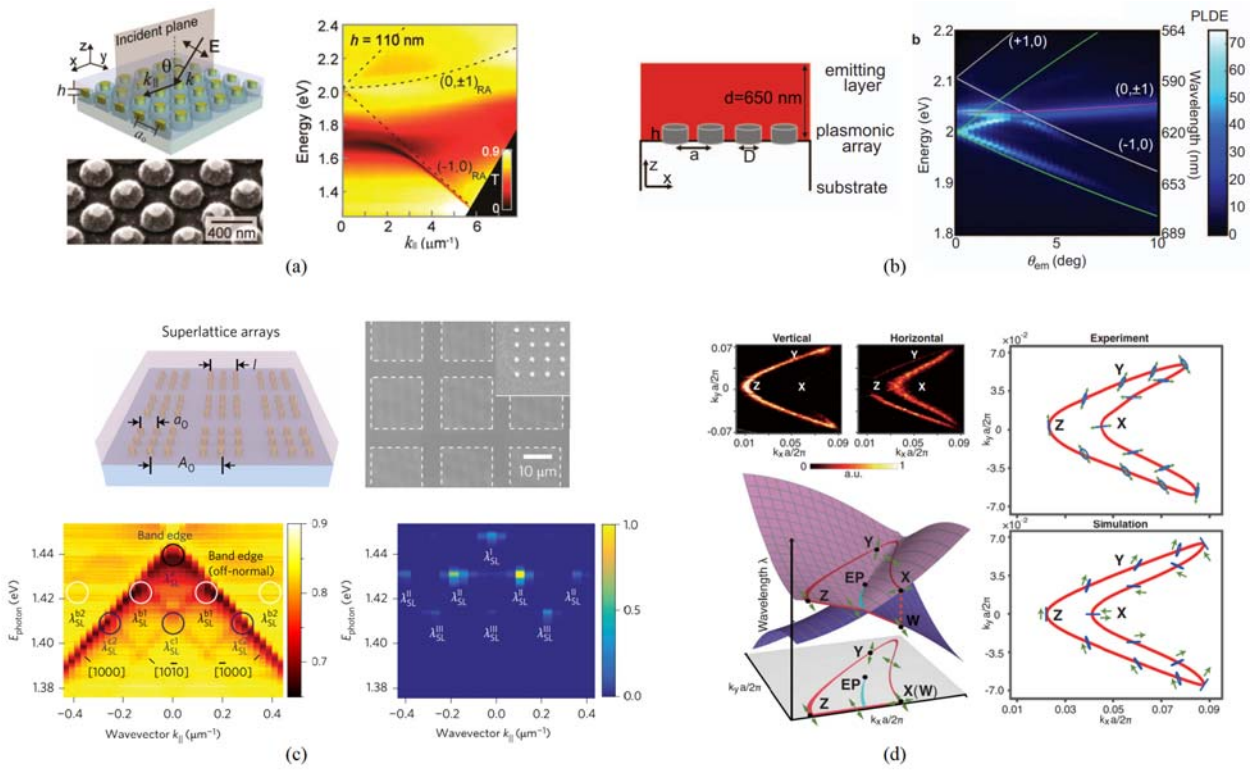

Fig. 1. ***Examples of periodic arrays of nanoscatterers, with properties determined by their photonic band structures. (a) Surface lattice resonances resulting from hybridization between localized resonances and RAs modify the optical response of 2-D array of plasmonic nanoparticles (left), giving rise to clear anticrossing signatures in the frequency-momentum dependence of the optical transmission (right). Reprinted from [27]. (b) Plasmonic arrays can be integrated into light-emitting devices (left) to improve the emission efficiency by diffractive outcoupling at RA. This is clearly evidenced by the photoluminescence directional enhancement (PLDE, right) measured as a function of photon energy (vertical axis) and emission angle (horizontal axis). Reprinted from [9]. (c) Example of band structure design for controlling the light emission of plasmonic lattice lasers: hierarchical periodic arrays (scheme: top left, SEM image: top right) feature multiple band edges (bottom left) that provide distributed feedback for simultaneous lasing at various wavelengths and in-plane momenta (bottom right). Reprinted from [28]. (d) Example of a nontrivial topology due to PT symmetry breaking in a non-Hermitian photonic crystal: polarization-resolved isofrequency contour of the scattered light (top left) around a pair of EPs show that the photonic bands (bottom left) have a fractional topological charge around each EP, which gives rise to the unique polarization signature (right). Reprinted from [29].***

This same geometry also has been shown to bring active media to lasing [Fig. 1(c)], where feedback is essentially distributed feedback by in-plane Bragg diffraction generated by scattering off the plasmonic resonators [3]. Recently, these structures have also been extended to the regime of strong light–matter coupling, where the lattices are coupled to dense excitonic media in which one hopes to observe collective effects, such as Bose condensation of hybrid exciton–polariton excitations [11]. In these structures, the "building blocks" are essentially resonant electric dipole scatterers, the focus is on their hybridization with diffraction conditions, and the open questions revolve around the interaction with active media to create directional sources, with enhanced spontaneous emission rates (Purcell effect) and brightness and with enhanced local fields for efficient pumping [12].

In the field of metamaterials and metasurfaces, very often, the view is more strongly geared toward subwavelength periodicities and encoding of remarkable physics through the response function of the building blocks in each unit cell [13]. Primary examples are artificial nanostructured sheets with a magnetic and chiral response (bianisotropic or magnetoelectric scattering lattices) [14]–[16] and the so-called Huygens and Kerker-condition metasurfaces [17]–[22]. Key questions are how the single-building block properties ultimately reflect in the lattice response, especially given that, at high densities, subradiant and superradiant collective modes to form could be expected. Inspired by topological condensed matter physics, several groups have noted that particular periodic lattices of plasmonic antennas, such as the honeycomb lattice, may offer band structures with nontrivial topological properties [23]–[26]. Here, solid-state physics transposes directly to optics if the tight-binding approximation (nearest-neighbor and instantaneous interactions) is used, which is equivalent to the quasi-static approximation of plasmonics. AQ:2

Recently, another kind of topological properties [30]—associated with the non-Hermitian physics of periodic photonic systems—has attracted significant attention.

The most exciting ideas in this field involve parity-time (PT) symmetry and exceptional points (EPs). In the photonic context, PT symmetry can be understood as the hybridization of a pair of optical modes that are frequency-degenerate (have identical real eigenfrequencies) but differ in damping rates (have different imaginary eigenfrequencies). If the coupling is strong enough, the modes get separated in frequency and acquire identical damping rates, forming a PT-symmetric phase. If the initially uncoupled modes have exactly balanced gain and loss, the resulting hybridized modes would be lossless (purely real) and infinitely sharp. In the band structure of a lattice, the coupling strength varies as function of the parallel momentum. Therefore, in the momentum space of a periodic lattice, one may expect the emergence of a PT-broken phase [31], separated from the PT-symmetric phase by transition points (lines of EPs in the mometum space of 2-D lattices [32] and surfaces of EPs in 3-D [33]), at which the two complex-valued eigenmodes merge into one. EPs are very interesting from a fundamental viewpoint, as they challenge the Hamiltonian-based description of photonic systems by violating the completeness of the Hamiltonian basis [7], [34]. Furthermore, photonic bands around EPs have nontrivial Möbius strip-like topology, corresponding to a fractional topological charge [29]. At the same time, the singular character of EPs could be of potential use, e.g., for sensing [6], light shaping [32], and Purcell enhancement [35]. A popular strategy to achieve PT symmetry in periodic lattices is by spatially structuring the distributions of gain and loss on length scales of/within the unit cell [32], although to-date experimental demonstrations have exploited passive photonic crystals with accidentally degenerate multipolar modes of different radiative damping rates [29], [36]. Interestingly, both Hermitian (e.g., spin-Hall and valley-Hall effects) and non-Hermitian topological features (EPs and PT symmetry) can be identified by their polarization signatures [37] [Fig. 1(d)]: either in the scattered polarization state [29] or in the response to incident polarization [38]. EPs embedded in the polarization space (instead of the momentum space) have also been observed in THz metasurfaces by exploiting their anisotropic damping factor [39].

In view of the large importance of periodic 2-D arrays of very strongly scattering resonant subwavelength building blocks coupled to gain and loss, there is a large need for a theoretical framework that can act as a "minimal model." The requirements of a "minimal model" are that, on one hand, the model is sufficiently simple with essential physical ingredients such as the resonant response of single building blocks, and the lattice geometry is clearly tractable as semianalytical input; on the other hand, it should be sufficiently rigorous to provide access in a self-consistent way to the essential physical properties. This implies access to observables reflection, transmission, diffraction, absorption, local density of states (LDOSs), and band structure with a closed energy balance and also implies properly accounting for essential phenomena such as near-field and long-range electrodynamic interactions, retardation effects, subradiant damping, and superradiant damping. This idea of a "minimal model" should be juxtaposed against two complementary approaches. On the one hand, full-wave simulations are exact but intrinsically slow to evaluate and hard to interpret as these simulations are essentially numerical experiments. On the other hand, we require more of a "minimal model" than that is offered by, e.g., coupled oscillator and quasi-static hybridization approaches to describe plasmon particle systems. These approaches typically violate energy conservation (i.e., the optical theorem that states that extinction should equal the sum of absorption and scattering in the absence of gain), have no retarded, subradiant, and superradiant physics in them and are generally limited to nearest neighbor/tight-binding approximations. The method of choice that we review here is a multiple scattering method for dipolar and bianisotropic scatterers, where we account for multiple scattering to all orders by solid-state techniques for dealing with lattice interactions [8], [40]–[47]. Here we show its effectiveness as a minimal model for the optical response of strongly scattering lattices with loss and gain, giving access to the band structures, eigenmodes, and observable signatures of PT-symmetric systems.

This article is organized as follows. In Section II, we briefly review the theory of scattering from individual resonant nanoparticles, including the effects associated with optical gain. Section III elaborates on lattices, providing a self-consistent tutorial on the calculations of the effective polarizability and reflection/transmission as a function of frequency and in-plane component of the momentum. Both Sections II and III provide a comprehensive and didactic description of the basic and general theory that can be used to model a rich variety of optical systems. Experts in the field are encouraged to read these Sections only cursorily and focus their attention on Section IV that presents example results of our ongoing research in a new application domain, namely, on plasmonic arrays with gain and loss, showing the capability of Green function methods to study PT symmetry and nontrivial properties of EPs.

II. OPTICAL RESPONSE OF A SINGLE SCATTERER

This section briefly reviews the general theory of light scattering by individual nanoparticles in the frame of classical linear frequency-domain electrodynamics, discussing the most basic aspects of this phenomenon such as bianisotropy, energy conservation, absorption, scattering, extinction, plasmon resonance, and gain. Readers familiar with these aspects are encouraged to focus on Section III, which provides a tutorial on multiple scattering in nanoparticle arrays (based on theory consistent with Section II), or to move directly to Section IV, which contains new results related to PT symmetry.

A. Point-Dipole Polarizability Tensor

The main approximation of our method is to approximate the response of single scatterers by a single-point dipole polarizability [48]–[51], where we treat electric and magnetic dipoles on equal footing. Thus, the optical response is approximated by a 6-vector of the electric and magnetic dipoles $\mathbf{P}$ induced by the incident electromagnetic fields $\mathbf{F}_{\text{in}}$

$$\mathbf{P} = \alpha \mathbf{F}_{\text{in}}. \tag{1}$$

Here and throughout the entire article, we will use a modified system of units for $\mathbf{P}$, $\boldsymbol{\alpha}$ and $\mathbf{F}_{\text{in}}$ (conversion from SI, Appendix V) to ensure elegant symmetry between the electric and magnetic terms. We express $\mathbf{P}$ and $\mathbf{F}_{\text{in}}$ as six-element vectors of Cartesian components of the induced electric and magnetic dipoles and fields, respectively,

$$\mathbf{P} = \begin{pmatrix} \mathbf{p} \\ \mathbf{m} \end{pmatrix} = \begin{pmatrix} p_x \\ p_y \\ p_z \\ m_x \\ m_y \\ m_z \end{pmatrix}, \quad \mathbf{F}_{\text{in}} = \begin{pmatrix} \mathbf{E}_{\text{in}} \\ \mathbf{H}_{\text{in}} \end{pmatrix} = \begin{pmatrix} E_{x,\text{in}} \\ E_{y,\text{in}} \\ E_{z,\text{in}} \\ H_{x,\text{in}} \\ H_{y,\text{in}} \\ H_{z,\text{in}} \end{pmatrix}. \tag{2}$$

Equation (1) must, therefore, contain a 6×6 polarizability matrix $\boldsymbol{\alpha}$, which, in the most general case, can be expressed as four 3×3 blocks

$$\boldsymbol{\alpha} = \begin{pmatrix} \boldsymbol{\alpha}_{\text{EE}} & \boldsymbol{\alpha}_{\text{EH}} \\ \boldsymbol{\alpha}_{\text{HE}} & \boldsymbol{\alpha}_{\text{HH}} \end{pmatrix} \tag{3}$$

where the diagonal blocks $\boldsymbol{\alpha}_{\text{EE}}$ and $\boldsymbol{\alpha}_{\text{HH}}$ are the electric and magnetic polarizability tensors, respectively, whereas the off-diagonal terms $\boldsymbol{\alpha}_{\text{EH}}$ and $\boldsymbol{\alpha}_{\text{HE}}$ are the so-called bianisotropic terms that describe the magnetoelectric coupling, i.e., the induction of electric dipoles by magnetic fields and magnetic dipoles by electric fields [52]–[55]. In plasmonics, generally $\boldsymbol{\alpha}_{\text{EE}}$ dominates over the other terms and describes the most common scattering systems. However, other terms may become significant in specially designed scattering objects, such as split-ring resonators, where the bianisotropic terms give rise to the so-called pseudochirality, i.e., direction-dependent scattering of right- and left-handed circularly polarized lights [14], [56].

The components of a realistic polarizability tensor cannot be chosen arbitrarily, as they are subject to Onsager constraints [52], [57], [58] without which reciprocity is violated

$$\boldsymbol{\alpha}_{\text{EE}} = \boldsymbol{\alpha}_{\text{EE}}^T, \quad \boldsymbol{\alpha}_{\text{HH}} = \boldsymbol{\alpha}_{\text{HH}}^T, \quad \boldsymbol{\alpha}_{\text{EH}} = -\boldsymbol{\alpha}_{\text{HE}}^T \tag{4}$$

where $(\dots)^T$ indicates a matrix transpose. Furthermore, if $\boldsymbol{\alpha}$ does not contain any loss or gain, equating the scattered power to the work done by the incident field imposes the following energy conservation formula originally due to Sipe and Van Kranendonk [59] and extended to bianisotropy by Belov *et al.* [53] and Sersic *et al.* [54]

$$\frac{1}{2i}[\boldsymbol{\alpha} - \boldsymbol{\alpha}^{*T}] = \frac{2}{3}k^3 \boldsymbol{\alpha}^{*T} \boldsymbol{\alpha} \tag{5}$$

where $(\dots)^*$ means the complex conjugation, $k = n\omega/c$ is the wavenumber, n is the refractive index, and c is the vacuum light speed. The above-mentioned theorem also enables to convert any magnetoelectrostatic 6×6 polarizability $\boldsymbol{\alpha}_{\text{stat}}$ (e.g., any static RLC-circuit-derived polarizability) into electromagnetically consistent dynamic polarizability $\boldsymbol{\alpha}_{\text{dyn}}$ [50], [51], [54] via

$$\boldsymbol{\alpha}_{\text{dyn}}^{-1} = \boldsymbol{\alpha}_{\text{stat}}^{-1} - \frac{2i}{3}k^3 \mathbb{I}_{6\times 6} \tag{6}$$

where $\mathbb{I}_{6\times 6}$ is the 6×6 identity matrix. The second term in the above equation introduces radiative damping, the inevitable consequence of interaction with continuous bath of optical states at infinity. Inserting this radiation damping converts any electrostatic model for a scatterer into one for which the optical theorem (extinction equals absorption plus scattering) is satisfied for any physical incidence condition.

If $\boldsymbol{\alpha}_{\text{dyn}}$ is diagonalizable, i.e., one can calculate its eigenvalues α_j ("eigenpolarizabilities") and the corresponding eigenvectors $\mathbf{v}_j$ ("eigenilluminations"), it can be shown that, in the absence of gain, $\text{Im}(\alpha_j)$ will always be positive, even for an intrinsically lossless scatterer (i.e., purely real $\boldsymbol{\alpha}_{\text{stat}}$). Furthermore, if $\boldsymbol{\alpha}_{\text{stat}}$ contains some off-diagonal magnetoelectric coupling terms $\boldsymbol{\alpha}_{\text{stat},EH,HE}$, the above-mentioned relation would impose an upper limit on their magnitude, which would depend on the product of the diagonal terms $\boldsymbol{\alpha}_{\text{stat},EE,HH}$ [54]. In addition, (6) leads to a generalized optical theorem for the eigenpolarizabilities

$$\text{Im}(\alpha_j) \geqslant \frac{2}{3}k^3 |\alpha_j|^2 \tag{7}$$

with strict equality for a lossless scatterer (the "unitary limit"). If $\boldsymbol{\alpha}_{\text{dyn}}$ is diagonal, (7) states that energy is conserved only when each tensor element satisfies the scalar optical theorem $\text{Im}(\alpha) \geqslant (2/3)k^3|\alpha|^2$. On the other hand, adding gain relaxes the above-mentioned constraints, allowing, e.g., negative $\text{Im}(\alpha_j)$, if the material gain overcomes all (radiative and material) losses. Inasfar as the eigenilluminations can be realized, the eigenpolarizabilities α_j are directly linked to experimental observables, i.e., to the scattering $\sigma_{\text{scat},j}$ and extinction cross sections $\sigma_{\text{ext},j}$

$$\sigma_{\text{scat},j} = \frac{8\pi}{3}k^4 |\alpha_j|^2, \quad \sigma_{\text{ext},j} = 4\pi k \,\text{Im}(\alpha_j) \tag{8}$$

which define the absorption cross section via $\sigma_{\text{abs},j} = \sigma_{\text{ext},j} - \sigma_{\text{scat},j}$ [48]. While $\sigma_{\text{scat},j}$ is always positive as it quantifies the amount of energy that is radiated away, negative $\text{Im}(\alpha_j)$ implies that $\sigma_{\text{abs},j}$ and $\sigma_{\text{ext},j}$ can also be negative. This means that, in the presence of gain, energy is added to the incident wave [60] instead of being subtracted from it. Note that ultimately, gain could lead to lasing. However, in our linear model, gain is not saturable, population inversion is not accounted for, and our model only reaches up to, but not beyond any lasing threshold.

B. Electrostatic Polarizability of Plasmonic Nanoparticles

Classical electrodynamics predicts an onset of optical resonances that may exist in a nanoparticle depending on the optical constants of the nanoparticle material and the surrounding medium, as well as on the nanoparticle size and shape [61], [62]. They can be classified into two main groups: localized surface plasmon resonances (LSPRs) and dielectric Mie resonances. Each group forms a sequence of multipolar modes: electric dipole, magnetic dipole, electric quadrupole, and so on. In most cases, subsequent resonances can only emerge in a nanoparticle that is sufficiently large compared to the optical wavelength. The notable exception is the dipolar LSPR, which is predicted in the electrostatic approximation. This resonance exists independently of the particle size, provided that the optical constants fulfill the resonance conditions governed by the dispersion of $\boldsymbol{\alpha}_{\text{stat},EE}$. For a spherical nanoparticle with electric permittivity ε_2 embedded in a medium ε_1 [51], [63]

$$\boldsymbol{\alpha}_{\text{stat},EE} = 3V\frac{\varepsilon_2 - \varepsilon_1}{\varepsilon_2 + 2\varepsilon_1}\mathbb{I}_{3\times 3} \tag{9}$$

where V is the nanoparticle volume and $\mathbb{I}_{3\times 3}$ is the 3×3 identity matrix. The resonance occurs at the so-called Fröhlich condition: $\varepsilon_2 = -2\varepsilon_1$, requiring that the nanoparticle and the surrounding medium have optical constants of opposite signs, i.e., one of them is metal and the other is dielectric. Calculation of $\boldsymbol{\alpha}_{\text{stat},EE}$ for arbitrary shapes typically requires numerical methods [48]; however, for certain simple shapes, it can be analytically derived [61], [62], [64], [65]. In this article, we will consider ellipsoidal core–shell geometries, described by formulas given in Appendix V.

LSPR originates from the frequency dependence (dispersion) of the optical constants. A common approach to accurately simulate optical properties of metals is to interpolate the experimental data, e.g., from Johnson and Christy [66]. On the other hand, these data are often approximated by the Drude model

$$\varepsilon_{\text{D}} = \varepsilon_\infty - \frac{\omega_p^2}{\omega^2 + i\omega\gamma} \tag{10}$$

where ε_∞ is the electric permittivity in the high-frequency limit, ω_p is the plasma frequency, and γ is the Drude damping coefficient. Drude model can be extended to the Lorentz–Drude model, which contains additional oscillator terms

$$\varepsilon_{\text{LD}} = \varepsilon_{\text{D}} - \omega_p^2\sum_{n=1}^{N}\frac{f_n}{\omega_n^2 - \omega^2 + i\omega\Gamma_n}. \tag{11}$$

For the examples presented in this article, we will use a custom fit of the optical constants of silver with only two Lorentz terms. Parameters of our model are: $\varepsilon_\infty = 5.3$, $\hbar\omega_p = 9.5$ eV, $\hbar\gamma = 0.013$ eV, $f_1 = 0.012$, $\hbar\omega_1 = 3.8$ eV, $\hbar\Gamma_1 = 1.1$ eV, $f_2 = 0.006$, $\hbar\omega_2 = 2.2$ eV, and $\hbar\Gamma_2 = 0.88$ eV. This fit nicely reproduces both real and imaginary parts of electric permittivity of silver in the spectral range of 1.4–3.7 eV, which covers the entire visible part of the spectrum. To cover a wider spectral range, more Lorentz terms can be added [67]. Since all calculations presented in this article are linear and in the frequency domain, we could use tabulated ε from the literature instead of Lorentz–Drude models. However, Lorentz–Drude models are useful for seamless comparison to possible extensions of our theory into the time domain, enabling studies of nonlinearity and ultrafast dynamics, which, under certain conditions, may be relevant for gain media discussed in the following.

C. Optical Properties of Gain Media

The simplest gain medium model is that of a two-level gain system [68]

$$\varepsilon_g = \varepsilon_{g0} + Q\frac{\gamma_g}{\omega_g - \omega + i\gamma_g} \tag{12}$$

where ε_{g0} is the permittivity of gain medium in the absence of gain, Q is a dimensionless constant that determines the gain magnitude, γ_g is the gain bandwidth, and ω_g is the central frequency of the stimulated optical transition. The imaginary part of ε_g may contain both a positive contribution from the losses encoded in ε_{g0}, and a negative contribution of the Lorentzian gain term. As can be noted, gain modifies not only the imaginary but also the real part of ε_g, as dictated by Kramers–Kronig relations. This leads to gain-induced changes of refractive index, a common effect observed in high-gain lasers as "gain-guiding" [69].

To get some intuition about the magnitude of gain, one can convert ε_g into the material gain coefficient g

$$g = 2k_0\sqrt{\frac{|\varepsilon_g| - \text{Re}(\varepsilon_g)}{2}} \approx -k_0\frac{\text{Im}(\varepsilon_g)}{n_{g0}} \tag{13}$$

where $k_0 = \omega/c = 2\pi/\lambda$ is the vacuum wavenumber, $|\varepsilon_g|$ is the modulus of ε_g, and $n_{g0} \approx \sqrt{\text{Re}(\varepsilon_{g0})}$ is the refractive index of the gain medium in the absence of gain (the approximation is valid under assumption that the medium

has negligible intrinsic losses). The coefficient g is given in the units of inverse length, usually cm^{-1}. If an infinite plane wave propagates through an infinite nondispersive homogeneous gain medium, then its intensity grows by a factor of $\exp(gz)$ after propagating along distance z. In confined systems, such as waveguides and microcavities, g should be replaced by the so-called modal gain coefficient g_{mod}, which is equal to g corrected by some specific "confinement factor" [70].

Optical gain can be introduced directly into the polarizability description of resonant nanoparticles, as in the theoretical work by Manjavacas [68], where the permittivity of nanoparticles was described by an equation similar to (12), but with ε_{g0} governed by a Drude model (i.e., $\varepsilon_{g0} \equiv \varepsilon_{\mathrm{D}}$). Such nanoparticles could support simultaneously a dipolar LSPR mode and gain at a coinciding wavelength. Here, we will consider a more conventional system based on core–shell nanoparticles, each with silver core ε_m and gain medium shell ε_g, embedded in passive and lossless dielectric medium ε_d. We will assume that, in the absence of gain, the gain medium that forms the shell is also a passive and lossless dielectric, i.e., $\varepsilon_{g0} = \mathrm{Re}(\varepsilon_{g0}) = n_g^2$. Fig. 2 shows the example spectral dependencies of cross sections calculated for a disk-shaped core–shell nanoparticle with various magnitudes of gain in the shell. We find that the nanoparticle can scatter more light than it receives ($\sigma_{\mathrm{ext}} < \sigma_{\mathrm{scat}}$) if g exceeds 5100 cm^{-1}.

To provide a perspective on this number, we note that this gain coefficient exceeds that achievable in most gain media. For instance, a typical material gain of laser dyes is ≈10 cm^{-1} [71], [72]. The highest values for organic media have been reported in conjugated polymers [73] and IR-140-doped polymethyl methacrylate (PMMA) [74], reaching ≈150 and 300 cm^{-1}, respectively. In rare-earth-doped glasses [75], colloidal quantum dots [76], and semiconductor amplifiers [77], maximal values of ≈240, 650, and 800 cm^{-1} have been reported, respectively. However, lead halide perovskite thin films [78] have been shown to reach ≈3000 cm^{-1}. Moreover, recently developed quantum-confined colloidal nanoplatelets [79] can reach up to 6600 cm^{-1} at room temperature. Even higher material gain of 10^4–10^5 cm^{-1} is achievable at cryogenic temperatures in bulk semiconductors [80] and epitaxial quantum dots [81].

Our calculations are purely classical and neglect any coupling between LSPR and energy levels of the gain medium. Detailed microscopic picture of such effects can be found elsewhere [82]. Furthermore, our description of gain is valid under two assumptions: first, that the gain is constant in time, and second, that the gain does not saturate. While optical pumping with a nanosecond laser could provide quasi-stationary gain that roughly meets the first condition, the second is more tricky. This is because a resonant nanoparticle inevitably acts like an optical cavity. If all losses of such a nanoscale cavity are overcome by gain, the system rapidly amplifies the local fields and

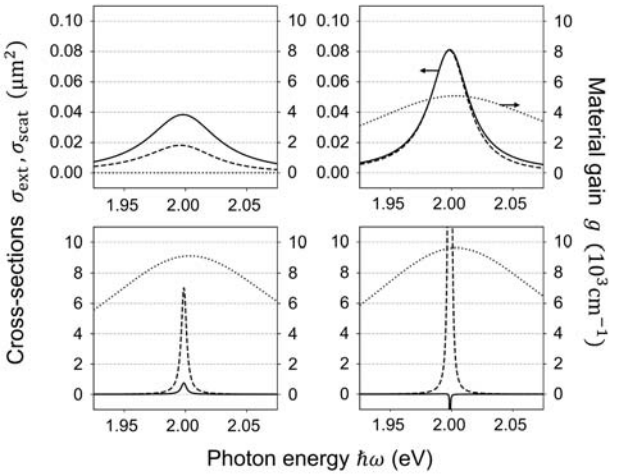

Fig. 2. *Optical properties of an ellipsoidal core–shell nanoparticle, with silver core modeled by $\varepsilon_m \equiv \varepsilon_{LD}$ from (11) and dimensions ≈ 18 nm ×18 nm × 6 nm (diameters along the symmetry axes), and gain medium shell modeled by $\varepsilon_{g0} = 4$, $\hbar\omega_g = 2$ eV, and $\hbar\gamma_g = 0.1$ eV, with outer diameters: 54 nm × 54 nm × 18 nm, embedded in a dielectric environment of refractive index $n_d = 1.5$. Solid lines: extinction cross section $\sigma_{ext,x}$. Dashed lines: scattering cross section $\sigma_{scat,x}$. Values of both cross sections are displayed on the left axis of each plot. Dotted lines: material gain coefficient g. Values of this coefficient are displayed on the right axes. Subsequent plots correspond to different magnitudes of material gain: Q = 0 (top left), Q = 0.1 (top right), Q = 0.18 (bottom left), and Q = 0.19 (bottom right). In the absence of gain $\sigma_{ext} > \sigma_{scat}$ (top left). In all cases, both cross sections are significantly larger than the geometrical cross section of nanoparticles under z-incidence (≈0.0023 μm^2), and they are further increased by adding gain. However, σ_{scat} grows faster, and it surpasses σ_{ext} around g ≈ 5100 cm^{-1} (top right). Up to g ≈ 9600 cm^{-1}, the nanoparticle scatters more energy than it receives (bottom left); however, σ_{ext} remains positive, meaning that the local field oscillations are decaying. When g exceeds 9600 cm^{-1}, σ_{ext} becomes negative, and the nanoparticle becomes a sparser (bottom right).*

becomes a spaser, i.e., plasmon laser [83]. In order to experience any gain in such system, the incident light has to interact with the scatterer before it becomes a spaser. From the experimental point of view, this requires a pump–probe configuration akin to the transient extinction measurements [84] with proper timing between pump and probe pulses (appropriate synchronization is also needed to separate the probe from amplified spontaneous emission). In this article, we will consider optical properties that could be observed precisely in such pump–probe configuration.

III. OPTICAL RESPONSE OF A LATTICE

Plasmonic lattices are often studied in two distinct regimes: the "diffractive" regime and the "near-field" regime. Both limits can be intuitively understood. In the diffractive regime, the distance between nanoparticles is greater or equal to the optical wavelength in the embedding medium, and so to first order, one could neglect

multiple scattering and consider each nanoparticle as an independent source of scattered light, excited by an incident wave ("Huygens principle") [20], [21]. In this "nearly free photon" picture, the periodic arrangement of scatterers folds the dispersion of the embedding medium into the light cone, leading to sharp resonances known as grating (Rayleigh) anomalies [12]. Upon coupling with the localized nanoparticle resonances (introducing multiple scattering corrections), these anomalies become "surface lattice resonances." Conversely, in the "near-field regime," the coupling between particles is very strong, while grating diffraction is forbidden. When the spacing between nanoparticles is below $\lambda/2\pi$, mainly their evanescent fields $1/r^3$ overlap. Such lattices are often described by tight-binding models [23]–[26], [85] with direct analogy to solid state physics of 2-D materials.

The above-mentioned limiting cases are not accurate for the intermediate regime, i.e., for nanoparticles distanced by a fraction of the optical wavelength: from about 50 to 500 nm. Although in such case they are no longer coupled by their near fields, they can strongly interact via multiple scattering [1], [8], [12], [27], [42], [45]. This happens especially when the scattering cross sections of individual nanoparticles are larger than the unit cell surface area. Radiative coupling between localized resonances of individual nanoparticles gives rise to collective modes, which we call lattice resonances. The linewidths of modes can be very different from the single-particle linewidth due to superradiant damping (collective modes with wave vector within the light cone) or subradiance (wave vector outside the light cone). This section introduces a minimal model that enables to study lattice resonances in such intermediate regime. We provide a rigorous theoretical framework that enables to simulate reflection, transmission, as well as dispersion of photonic bands, in lattices with complex unit cells hosting arbitrary arrangements of nanoparticles, each described by its own polarizability and gain/loss characteristics.

A. Effective Polarizability and Lattice Green Function

We now consider an ensemble of scatterers $l = 1, 2, 3 \ldots, N$ located at positions $\mathbf{r}_l$, which can form an arbitrary 3-D spatial arrangement. Under illumination by light, each nanoparticle will respond not only to the incident optical field $\mathbf{F}_{\text{in}}$ but also to the sum of the optical fields scattered by all other nanoparticles l' located at different positions $\mathbf{r}_{l'}$ [42], [48], [49]

$$\mathbf{P}_l = \boldsymbol{\alpha}_l \left[\mathbf{F}_{\text{in}}(\mathbf{r}_l) + \sum_{l'=1,\, l' \neq l}^{N} \mathbf{G}^0(\mathbf{r}_l - \mathbf{r}_{l'}) \mathbf{P}_{l'} \right] \tag{14}$$

where $\boldsymbol{\alpha}_l$ is the dynamic polarizability of nanoparticle l defined in (6), $\mathbf{F}_{\text{in}}(\mathbf{r}_l)$ is the incident field at position $\mathbf{r}_l$, whereas $\mathbf{G}^0(\mathbf{r}_l - \mathbf{r}_{l'})$ is the 6×6 dyadic point-dipole Green function of the embedding medium. It can be expressed in a more general form as $\mathbf{G}^0(\mathbf{r} - \mathbf{r}')$, describing the electromagnetic fields at $\mathbf{r}$ created by a point dipole at $\mathbf{r}'$ [50], [51]

$$\mathbf{G}^0(\mathbf{r} - \mathbf{r}') = \begin{pmatrix} \mathbb{I}_{3\times 3} k^2 + \nabla \otimes \nabla & -ik\nabla \times \\ ik\nabla \times & \mathbb{I}_{3\times 3} k^2 + \nabla \otimes \nabla \end{pmatrix} \frac{e^{ik|\mathbf{r}-\mathbf{r}'|}}{|\mathbf{r} - \mathbf{r}'|} \tag{15}$$

where $\otimes$ is the outer product of two vectors.

Having defined the mutual spatial arrangement of nanoparticles $\mathbf{r}_l$ and their individual polarizabilities $\boldsymbol{\alpha}_l$, we now repeat this ensemble along the 2-D lattice vectors $\mathbf{R}_{m,n} = m\mathbf{a}_1 + n\mathbf{a}_2$, where $\mathbf{a}_i$ are the lattice basis vectors. In this way, we create a complex lattice that can be thought as a stack of primitive sublattices $\mathbf{r}_{l,m,n} = \mathbf{r}_l + \mathbf{R}_{m,n}$, $m, n = \ldots, -2, -1, 0, 1, 2, \ldots$, where $\mathbf{r}_l$ is short for $\mathbf{r}_{l,0,0}$, denoting the origin of sublattice l.

If we assume that the lattice is illuminated by a plane wave of momentum $\mathbf{k}$ and otherwise fully specified by its value $\mathbf{F}_0$ at the origin, the incident field acting on the scatterers can be expressed as

$$\begin{aligned} \mathbf{F}_{\text{in}}(\mathbf{r}_{l,m,n}) &= \mathbf{F}_0 e^{i\mathbf{k}\cdot\mathbf{r}_{l,m,n}} \\ &= \mathbf{F}_0 e^{i\mathbf{k}_{||}\cdot\mathbf{R}_{m,n} + i\mathbf{k}\cdot\mathbf{r}_l} \end{aligned} \tag{16}$$

where $\mathbf{k}_{||}$ is the projection of $\mathbf{k}$ on the lattice plane. At the same time, Bloch's theorem guarantees that one can write the solution as

$$\mathbf{P}_{l,m,n} = \mathbf{P}_l \, e^{i\mathbf{k}_{||}\cdot\mathbf{R}_{m,n}} \tag{17}$$

where now $\mathbf{P}_l$ is shorthand for $\mathbf{P}_{l,0,0}$, i.e., the dipole moment at the origin of sublattice l, which can be expressed as

$$\mathbf{P}_l = \boldsymbol{\alpha}_l \Bigg[\mathbf{F}_0 e^{i\mathbf{k}\cdot\mathbf{r}_l} + \mathcal{G}^{\neq}(\mathbf{k}_{||}, \mathbf{r}_0)\mathbf{P}_l + \sum_{l'=1,\, l' \neq l}^{N} \mathcal{G}(\mathbf{k}_{||}, \mathbf{r}_l - \mathbf{r}_{l'})\mathbf{P}_{l'} \Bigg] \tag{18}$$

where $\mathcal{G}^{\neq}(\mathbf{k}_{||}, \mathbf{r}_0)$ and $\mathcal{G}(\mathbf{k}_{||}, \mathbf{r}_l - \mathbf{r}_{l'})$ are the "lattice sums" describing the intrasublattice and intersublattice interactions, respectively [44], [46]. Evaluation of $\mathcal{G}^{\neq}(\mathbf{k}_{||}, \mathbf{r}_0)$ involves summation of the point-dipole Green function $\mathbf{G}^0$ over all positions of the lattice nodes except the origin ($\mathbf{R}_{m,n} \neq \mathbf{R}_{0,0}$)

$$\mathcal{G}^{\neq}(\mathbf{k}_{||}, \mathbf{r}_0) = \sum_{m\neq 0,\, n\neq 0} \mathbf{G}^0(\mathbf{r}_0 - \mathbf{R}_{m,n}) e^{i\mathbf{k}_{||}\cdot\mathbf{R}_{m,n}} \tag{19}$$

where $\mathbf{r}_0$ is the observation point located exactly at the nanoparticle that constitutes the lattice origin, hence $\mathbf{r}_0 = \mathbf{R}_{0,0} = (0,0,0)^T$. On the other hand, $\mathcal{G}(\mathbf{k}_{||}, \mathbf{r}_l - \mathbf{r}_{l'})$ accounts for the interaction of the nanoparticle at the origin of sublattice l with all nanoparticles from sublattice l'; hence, it is calculated using the same formula but also including the origin $\mathbf{R}_{0,0}$

$$\mathcal{G}(\mathbf{k}_{||}, \mathbf{r}_l - \mathbf{r}_{l'}) = \sum_{m,n} \mathbf{G}^0(\mathbf{r}_l - \mathbf{r}_{l'} - \mathbf{R}_{m,n}) e^{i\mathbf{k}_{||}\cdot\mathbf{R}_{m,n}}. \quad (20)$$

Technical details on performing summations (19) and (20) are given in Appendix V.

Importantly, the structure of the equation that sets all dipole moments in the unit cell is a generalized form of our starting definition of polarizability, meaning that (18) can be recast into

$$\mathbf{P} = \boldsymbol{\alpha}_{\text{eff}} \mathbf{F}_{\text{in}} \quad (21)$$

where $\boldsymbol{\alpha}_{\text{eff}}$ now is a $6N \times 6N$ effective polarizability tensor for the N scatterers per unit cell, and $\mathbf{P}$ and $\mathbf{F}_{\text{in}}$ are the $6N$-element vectors for the N-induced dipoles and the driving fields applied to them, that is,

$$\mathbf{P} = \begin{pmatrix} \mathbf{P}_1 \\ \vdots \\ \mathbf{P}_l \\ \vdots \\ \mathbf{P}_N \end{pmatrix}, \qquad \mathbf{F}_{\text{in}} = \begin{pmatrix} \mathbf{F}_0 e^{i\mathbf{k}\cdot\mathbf{r}_1} \\ \vdots \\ \mathbf{F}_0 e^{i\mathbf{k}\cdot\mathbf{r}_l} \\ \vdots \\ \mathbf{F}_0 e^{i\mathbf{k}\cdot\mathbf{r}_N} \end{pmatrix}. \quad (22)$$

The effective polarizability is

$$\boldsymbol{\alpha}_{\text{eff}} = \left(\boldsymbol{\alpha}^{-1} - \mathscr{G}_{\text{latt}}\right)^{-1} \quad (23)$$

where $\boldsymbol{\alpha}$ is a block-diagonal matrix encoding the dynamic polarizabilities of all scatterers

$$\boldsymbol{\alpha} = \mathbb{I}_{N\times N}(\boldsymbol{\alpha}_1, \ldots, \boldsymbol{\alpha}_l, \ldots, \boldsymbol{\alpha}_N) \quad (24)$$

and the complete $6N \times 6N$ lattice Green function $\mathscr{G}_{\text{latt}}$ reads

$$\mathscr{G}_{\text{latt}} = \mathscr{G}_{\text{intra}} + \mathscr{G}_{\text{inter}} \quad (25)$$

with block-diagonal tensor $\mathscr{G}_{\text{intra}}$ for the intrasublattice interactions ($\otimes$ denoting the Kronecker product of two matrices)

$$\mathscr{G}_{\text{intra}} = \mathbb{I}_{N\times N} \otimes \mathcal{G}^{\neq}(\mathbf{k}_{||}, \mathbf{r}_0) \quad (26)$$

and block-off-diagonal tensor $\mathscr{G}_{\text{inter}}$ for the intersublattice interactions

$$\mathscr{G}_{\text{inter}} = \begin{pmatrix} 0 & \mathcal{G}_{1,2} & \cdots & \mathcal{G}_{1,l} & \cdots & \mathcal{G}_{1,N} \\ \mathcal{G}_{2,1} & 0 & \cdots & \mathcal{G}_{2,l} & \cdots & \mathcal{G}_{2,N} \\ \vdots & \vdots & \ddots & \vdots & & \vdots \\ \mathcal{G}_{l,1} & \mathcal{G}_{l,2} & \cdots & 0 & \cdots & \mathcal{G}_{l,N} \\ \vdots & \vdots & & \vdots & \ddots & \vdots \\ \mathcal{G}_{N,1} & \mathcal{G}_{N,2} & \cdots & \mathcal{G}_{N,l} & \cdots & 0 \end{pmatrix} \quad (27)$$

where $\mathcal{G}_{l,l'}$ is short for $\mathcal{G}(\mathbf{k}_{||}, \mathbf{r}_{l'} - \mathbf{r}_l)$. The above terms (26)–(27) are essential for the emergence of lattice resonances, encoding the full information on the lattice geometry and electromagnetic interactions. At the same time, they are completely independent of the optical properties of individual nanoparticles, which are encoded in $\boldsymbol{\alpha}$. While the model described earlier has mainly seen use in literature for primitive lattices (one nanoparticle per unit cell, setting $N = 1$ and $\mathscr{G}_{\text{inter}} = 0$) to match the majority of experiments on plasmon arrays, in fact, it allows to describe an overwhelming variety of nontrivial structures if one allows $N > 1$ scatterers per unit cell. This includes nontrivial 2-D lattices (honeycomb, Kagome, etc.), gradient metasurfaces with large unit cells containing closely spaced, distinct, building blocks [86], as well as systems that approach bulk metamaterials by stacking 2-D lattices one behind the other in the third dimension.

To illustrate the physics contained in the lattice sums, and in the effective polarizability of a lattice, we present the honeycomb lattice as a simple example of a nonprimitive lattice, equivalent to stacking $N = 2$ hexagonal sublattices A and B, with $\mathbf{a}_1 = a(1,0,0)^T$, $\mathbf{a}_2 = a((1/2),(\sqrt{3}/2),0)^T$ and $\mathbf{r}_{\text{B}} - \mathbf{r}_{\text{A}} = a((1/2),(\sqrt{3}/6),0)^T$, where a is the lattice period. Due to its analogy to graphene, the honeycomb lattice is particularly interesting as the starting point for topological [23]–[26], [87] and non-Hermitian physics [88]–[93]. Nontrivial phenomena occur mainly at the K points of the first Brillouin zone. In diffractive honeycomb arrays, these high-symmetry points correspond to the intersections of multiple Rayleigh anomalies (RAs) and, therefore, have recently been used for plasmonic-distributed feedback lasing [94]. Here, we will be interested in conical band degeneracies—Dirac points [95]—that are formed by lattice resonances in these k-space regions [96].

Fig. 3 shows the examples of the diagonal (intrasublattice) and off-diagonal (intersublattice) elements of the electric part of $\mathscr{G}_{\text{latt}}$, plotted as a function of frequency (on the vertical axis, expressed as photon energy $\hbar\omega$ in eV) and x component of the in-plane momentum $\mathbf{k}_{||}$ (horizontal axis). Each plot shows clear signatures of repeated dispersion relations (light cone edges) from the neighboring Brillouin zones. These sharp features give rise to RAs and to subsequent diffracted orders in the optical response of plasmonic lattice. Fig. 4 shows the

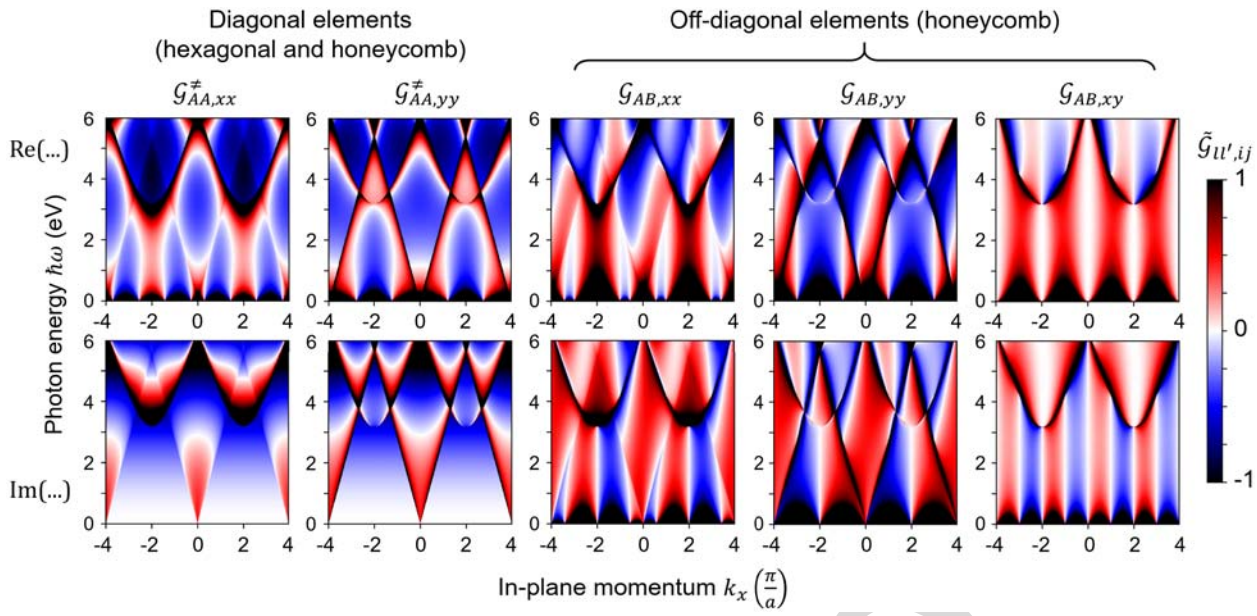

Fig. 3. *Elements of the electric part of the dyadic point-dipole lattice Green tensor $\mathcal{G}_{latt}$, calculated as a function of frequency ω (expressed as photon energy $\hbar\omega$) and in-plane momentum k_x (with fixed $k_y = 0$) for the honeycomb lattice with pitch $a = 150$ nm, assuming a dielectric environment of refractive index $n_d = 1.5$. The first Brillouin zone spans from −4/3 to 4/3 in the horizontal axis of each plot (k-space trajectory K′−Γ−K). The color scale represents the values of real (top row) and imaginary part (bottom row) of $\tilde{\mathcal{G}}_{ll',ij} = \mathcal{G}_{ll',ij}\sqrt{S^3}/(4\pi ka)$, where $S = |\mathbf{a_1} \times \mathbf{a_2}| \approx 0.02$ μm^2 is the unit cell surface area, and $k = n_d\omega/c$ is the wavenumber in the dielectric medium. Diagonal elements (intrasublattice terms $\mathcal{G}^{\neq}_{AA,ij}$, first four plots on the left) are identical in honeycomb and hexagonal lattices, whereas offdiagonal elements (intersublattice terms $\mathcal{G}_{AB,ij}$, six plots on the right) exist only in the honeycomb lattice, where they determine the interactions between sublattice A and sublattice B.*

resulting effective polarizability (23) of the unit cell for this lattice, as can be obtained once a scatterer polarizability is specified. As a simple example, we assume that the nanoparticles forming the honeycomb lattice are identical silver ellipsoids (without shell), embedded in a dielectric medium. Plots in the left column in Fig. 4 show the sum of static electric eigenpolarizabilities ($\sum_j \alpha_{\mathrm{stat},EE,j}$) of each individual nanoparticle, excluding the effect of radiation damping. Plots in the right column in Fig. 4 show the sum of effective lattice eigenpolarizabilities ($\sum_j \alpha_{\mathrm{eff},EE,j}$). As we can see, static polarizabilities (which initially do not depend on $k_{||}$) mix with the lattice Green function shown in Fig. 3, giving rise to dispersive lattice resonances. Here, we deliberately choose the size of the nanoparticles (36 nm diameter, 12 nm thickness) such that their scattering cross sections ($\sigma_{\mathrm{scat},x} \approx 0.04$ μm^2) noticeably exceeds the unit cell surface area ($S \approx 0.02$ μm^2), leading to significant dispersion and hybridization due to strong multiple scattering.

B. Reflection and Transmission

The advantage of the Green function method is the capability of *quantitative* evaluation of the scattered fields under plane wave illumination, assessing the experimental observables that include full information on the amplitude, phase, and polarization of the reflected, transmitted, and diffracted optical fields.

Once the induced dipole moments $\mathbf{P}$ are calculated by (21), the near-field distribution of the scattered optical fields $\mathbf{F}_{\mathrm{s}}^{(\mathrm{near})}(\mathbf{r})$ can be obtained from

$$\mathbf{F}_{\mathrm{s}}^{(\mathrm{near})}(\mathbf{r}) = \sum_{l=1}^{N} \mathcal{G}(\mathbf{k}_{||}, \mathbf{r} - \mathbf{r}_l)\mathbf{P}_l. \tag{28}$$

The total fields in the near-field zone $\mathbf{F}^{(\mathrm{near})}$ are the sum of the incident and the scattered fields

$$\mathbf{F}^{(\mathrm{near})}(\mathbf{r}) = \mathbf{F}_{\mathrm{in}}(\mathbf{r}) + \mathbf{F}_{\mathrm{s}}^{(\mathrm{near})}(\mathbf{r}). \tag{29}$$

The far-field distribution of the scattered optical fields $\mathbf{F}_{\mathrm{s}}^{(\mathrm{far})}(\mathbf{r})$ can be expressed as the sum of all nonevanescent diffracted orders $\tilde{m}, \tilde{n} = \ldots, -2, -1, 0, 1, 2, \ldots$

$$\mathbf{F}_{\mathrm{s}}^{(\mathrm{far})}(\mathbf{r}) = \sum_{\tilde{m},\tilde{n}} \mathbf{F}_{\tilde{m},\tilde{n}}\, e^{i\mathbf{k}_{\tilde{m},\tilde{n}}\cdot\mathbf{r}}. \tag{30}$$

Similar to (29), the total optical fields in the far-field zone $\mathbf{F}^{(\mathrm{far})}$ are equal to the sum of the incident and the scattered fields

$$\mathbf{F}^{(\mathrm{far})}(\mathbf{r}) = \mathbf{F}_{\mathrm{in}}(\mathbf{r}) + \mathbf{F}_{\mathrm{s}}^{(\mathrm{far})}(\mathbf{r}). \tag{31}$$

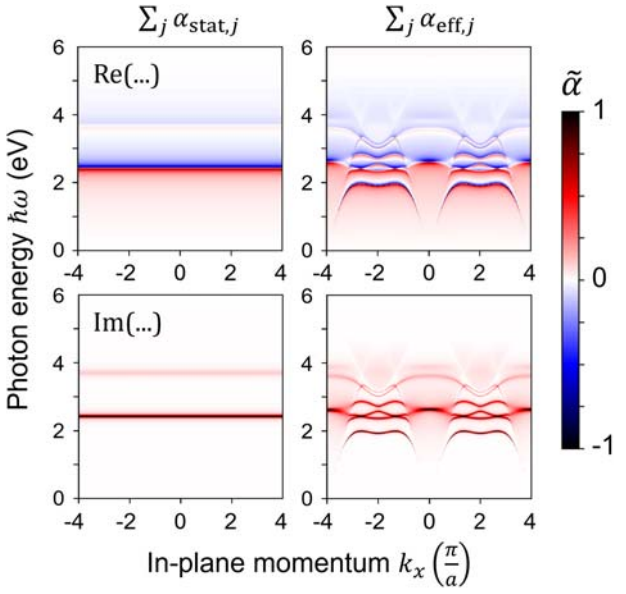

Fig. 4. *Sum of eigenvalues of α_{stat} of isolated nanoparticles (left column), and sum of eigenvalues of α_{eff} of the honeycomb lattice (right column), calculated as a function of frequency ω and in-plane momentum k_x (with fixed $k_y = 0$) for the honeycomb lattice with pitch $a = 150$ nm, composed of silver ellipsoids of dimensions $\approx$36 nm $\times$ 36 nm $\times$ 12 nm, embedded in a dielectric environment of refractive index $n_d = 1.5$. The color scale represents the values of real (top row) and imaginary part (bottom row) of $\tilde{\alpha} = 4 \times 10^{-4} \pi k a \sum_j \alpha_j / V$, where V is the nanoparticle volume, and $k = n_d \omega / c$. Static polarizabilities do not depend on $k_{||}$ (left column); however, they mix with lattice Green function shown in Fig. 3, giving rise to dispersive lattice resonances (right column). The number of photonic bands (appearing in the bottom right plot) is equal to the number of nonzero eigenvalues of α_{stat} multiplied by N—the number of scatterers per unit cell (i.e., the number of sublattices in the complex lattice). Hence, we get $2 \times 3 = 6$ bands because the honeycomb lattice has $N = 2$ sublattices, and in the given example, it is composed of silver ellipsoids that have three Cartesian elements of electric dipolar polarizability (two of which—along the in-plane directions x and y—are degenerate at $\hbar\omega \approx 2.4$ eV, whereas the third one—along the out-of-plane direction z—is blue-shifted to 3.7 eV). Due to the approximate treatment of the permittivity of silver and negligence of the dispersion of dielectric medium, the presented k-ω maps are quantitatively accurate only in the spectral range of 1.4–3.7 eV.*

In fact, the incident fields are added only to the zero-order transmission (i.e., the forward-scattered diffracted order with $\tilde{m} = 0, \tilde{n} = 0$), whereas the contributions of all other diffracted orders $\tilde{m}, \tilde{n}$ are exactly equal to the contributions of the corresponding scattered fields.

From the momentum conservation, the wave vector $\mathbf{k}_{\tilde{m},\tilde{n}}$ of each subsequent diffracted order $\tilde{m}, \tilde{n}$ can be expressed as

$$\mathbf{k}_{\tilde{m},\tilde{n}} = k \begin{pmatrix} \tilde{x} \\ \tilde{y} \\ \tilde{z} \end{pmatrix} \tag{32}$$

with in-plane and out-of-plane components

$$k(\tilde{x}, \tilde{y})^T = \mathbf{k}_{||} + \mathbf{K}_{\tilde{m},\tilde{n}} \tag{33}$$

$$k\tilde{z} = \pm\sqrt{k^2 - |\mathbf{k}_{||} + \mathbf{K}_{\tilde{m},\tilde{n}}|^2} \tag{34}$$

where "$\pm$" indicates the out-of-plane scattering direction ("+" for the forward, and "−" for the backward scattering, respectively), whereas $\mathbf{K}_{\tilde{m},\tilde{n}} = \tilde{m}\mathbf{b}_1 + \tilde{n}\mathbf{b}_2$ is the lattice momentum for a given diffracted order $\tilde{m}, \tilde{n}$, defined as the integer combination of the reciprocal lattice vectors $\mathbf{b}_j$, obtained from the real-space basis vectors through $\mathbf{a}_i \cdot \mathbf{b}_j = 2\pi\delta_{ij}$, where δ_{ij} is the Kronecker delta. Note that that $\tilde{x}, \tilde{y}$, and $\tilde{z}$ are always assigned to a specific diffracted order $\tilde{m}, \tilde{n}$.

Now the diffracted fields can be written as

$$\mathbf{F}_{\tilde{m},\tilde{n}} = \frac{2\pi k i}{S\tilde{z}} \mathbf{M}_{\tilde{m},\tilde{n}} \sum_{l=1}^{N} \mathbf{P}_l \, e^{-i\mathbf{k}_{\tilde{m},\tilde{n}} \cdot \mathbf{r}_l} \tag{35}$$

where $S = |\mathbf{a}_1 \times \mathbf{a}_2|$ is the surface area of the unit cell, and $\mathbf{M}_{\tilde{m},\tilde{n}}$ is the far-field matrix obtained by performing derivations in (15) and keeping only the far-field terms proportional to $|\mathbf{r} - \mathbf{r}'|^{-1}$

$$\mathbf{M}_{\tilde{m},\tilde{n}} = \begin{pmatrix} \mathbf{D}_{\tilde{m},\tilde{n}} & \mathbf{O}_{\tilde{m},\tilde{n}} \\ -\mathbf{O}_{\tilde{m},\tilde{n}} & \mathbf{D}_{\tilde{m},\tilde{n}} \end{pmatrix} \tag{36}$$

where

$$\mathbf{D}_{\tilde{m},\tilde{n}} = \begin{pmatrix} 1 - \tilde{x}^2 & -\tilde{x}\tilde{y} & -\tilde{x}\tilde{z} \\ -\tilde{x}\tilde{y} & 1 - \tilde{y}^2 & -\tilde{y}\tilde{z} \\ -\tilde{x}\tilde{z} & -\tilde{y}\tilde{z} & 1 - \tilde{z}^2 \end{pmatrix}$$

and

$$\mathbf{O}_{\tilde{m},\tilde{n}} = \begin{pmatrix} 0 & -\tilde{z} & \tilde{y} \\ \tilde{z} & 0 & -\tilde{x} \\ -\tilde{y} & \tilde{x} & 0 \end{pmatrix}.$$

The phase factor in (35) accounts for the far-field retardation between different sublattices. More details on the derivations of the above-mentioned expressions can be found in [44] and [97].

The out-of-plane momentum [the last term in (32)] must be real-valued in order to generate nonvanishing scattered fields in the far zone, which means that the summation in (30) must include only those diffracted orders $\tilde{m}, \tilde{n}$, for which

$$|\mathbf{k}_{||} + \mathbf{K}_{\tilde{m},\tilde{n}}| = \sqrt{\tilde{x}^2 + \tilde{y}^2} \leqslant k. \tag{37}$$

This constraint allows assigning a specific diffraction angle to each diffracted order $\tilde{m}, \tilde{n}$ by expressing $\mathbf{k}_{\tilde{m},\tilde{n}}$ in

spherical coordinates (θ, ϕ)

$$\frac{\mathbf{k}_{\tilde{m},\tilde{n}}}{k} = \begin{pmatrix} \tilde{x} \\ \tilde{y} \\ \tilde{z} \end{pmatrix} = \begin{pmatrix} \cos\phi \sin\theta \\ \sin\phi \sin\theta \\ \cos\theta \end{pmatrix}. \tag{38}$$

Now, the transmitted and reflected far-field intensities ($I_{\text{tran}}(\theta,\phi)$ and $I_{\text{refl}}(\theta,\phi)$, respectively) can be obtained from the electromagnetic fields calculated using (30)–(31)

$$\begin{aligned} I_{\text{tran}}(\theta,\phi) &= -\frac{\text{Re}\left[\mathbf{E}^{(\text{far})}(\theta,\phi) \times \mathbf{H}^{(\text{far})}(\theta,\phi)\right] \cdot \hat{\mathbf{z}}}{2Z} \\ I_{\text{refl}}(\theta,\phi) &= \frac{\text{Re}\left[\mathbf{E}_{\text{s}}^{(\text{far})}(\pi-\theta,\phi) \times \mathbf{H}_{\text{s}}^{(\text{far})}(\pi-\theta,\phi)\right] \cdot \hat{\mathbf{z}}}{2Z} \end{aligned} \tag{39}$$

where $(\mathbf{E}^{(\text{far})}, \mathbf{H}^{(\text{far})})^T = \mathbf{F}^{(\text{far})}$ and $(\mathbf{E}_{\text{s}}^{(\text{far})}, \mathbf{H}_{\text{s}}^{(\text{far})})^T = \mathbf{F}_{\text{s}}^{(\text{far})}$ are the electric and magnetic far-field components of the optical fields, and $Z = \sqrt{\varepsilon/\mu}$ is the embedding medium impedance. The same expressions can be applied to investigate the intensity of each diffracted order $\tilde{m}, \tilde{n}$ separately by picking only one element of the sum in (30) at a time, keeping in mind that only the zero-order transmission should contain the incident fields, i.e., it is evaluated using $\mathbf{F}^{(\text{far})}$ from (31), whereas all other diffracted intensities (both forward- and backward-scattered) are evaluated using $\mathbf{F}_{\text{s}}^{(\text{far})}$ from (30).

Fig. 5 shows the examples of calculated zero-order transmissivities T_{00} and reflectivities R_{00} for the same lattice as shown in Fig. 4 (honeycomb lattice of silver ellipsoids), illuminated by linearly s- and p-polarized light (top and middle, respectively), and by circularly polarized light (bottom). These values are simply obtained by dividing I_{tran} and I_{refl} by the incident intensity $I_{\text{in}} = -\text{Re}(\mathbf{E}_{\text{in}} \times \mathbf{H}_{\text{in}}) \cdot \hat{\mathbf{z}}/2Z$. The momentum of incident and outgoing light is limited to the light cone; hence, all areas outside the light cone appear dark. On the other hand, some lattice resonances intersect the light cone, giving rise to clear signatures in the observable reflection and transmission. These are the lattice resonances studied in several groups for the purpose of plasmon-array-enhanced solid-state lighting, lasing, and strong coupling [98]–[104].

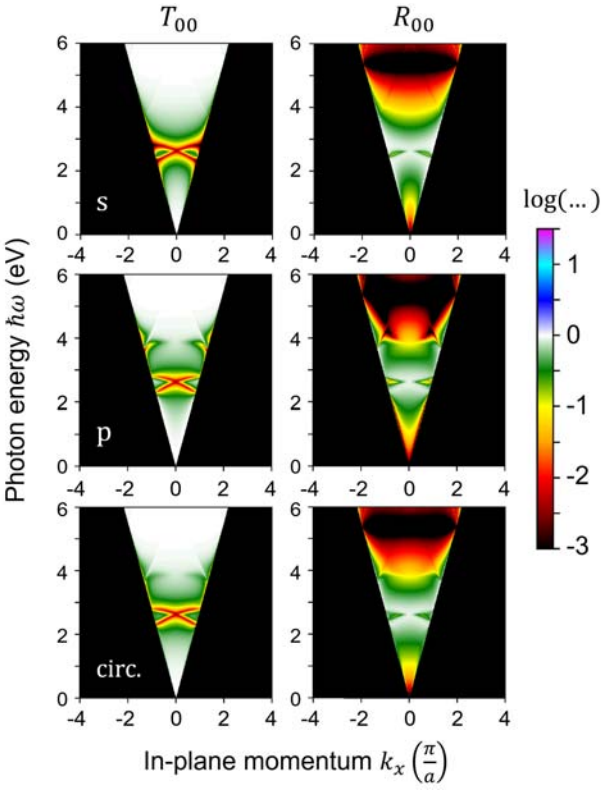

Fig. 5. *Zero-order transmissivity T_{00} (left column) and reflectivity R_{00} (right column) of the honeycomb lattice of silver disk-shaped ellipsoids (the same as in Fig. 4) illuminated either by a plane wave of linear s (top row), linear p (middle row), or circular left-handed polarization (bottom row). The range of frequency ω and in-plane momentum k_x is the same as in Figs. 3 and 4 (with fixed $k_y = 0$). The first Brillouin zone spans from $-4/3$ to $4/3$ (K'–Γ–K trajectory) in the units of π/a, whereas the light cone is contained in $|k_x| < k$. Within the light cone, k_x can be converted to the incidence angle $\theta_{in} = \arccos(k_x/k)$ (the edge of the light cone corresponds to $\theta_{in} = 90°$). Outside the light cone, the scattered fields are evanescent because photonic modes have too large momentum to couple with any incident or outgoing light. Some lattice resonances intersect with the light cone and strongly modify T_{00} and R_{00} at the resonant wavelengths. The color scale is logarithmic, allowing for values much larger than 1; however, in the given example, all plotted values are in the range from 0 to 1 because there is no gain. Similar to Fig. 4, the values are quantitatively accurate only in the spectral range of 1.4–3.7 eV due to the limited validity of the permittivity model.*

C. Guided Modes

While the dark areas in Fig. 5 are not accessible from the far field, Fig. 4 clearly shows that these areas contain nontrivial band structure features. These features are strictly guided lattice resonances [45]. They can be probed experimentally only by artificially increasing parallel momentum, e.g., using a coupling prism in the attenuated total reflection geometry [105], via additional weak periodic perturbations that fold bands back into the light cone [44], [106], [107], or via near-field probing [108] or excitation [109], [110]. The guided-mode regime of the band structure may emulate certain properties of electronic bands in solid state matter [23]–[25], [96], especially the effects associated with spin [111]. It is of particular interest to unravel what kind of optical modes exist at each point in the k-ω space in terms of polarization, symmetry, or topology. Probing these properties using theoretical tools is relatively simple by projection of the lattice polarizability tensor on the subspace of interest.

To this end, we define a metric for the norm of any operator $\mathbf{A}$ within a subspace $\mathcal{V}$ spanned by just n normalized basis vectors $\mathbf{v}_i$ each of length $6N$ as

$$||\mathbf{A}||_{\mathcal{V}}^2 = \sum_i \langle \mathbf{v}_i | \mathbf{A}^\dagger \mathbf{A} | \mathbf{v}_i \rangle. \tag{40}$$

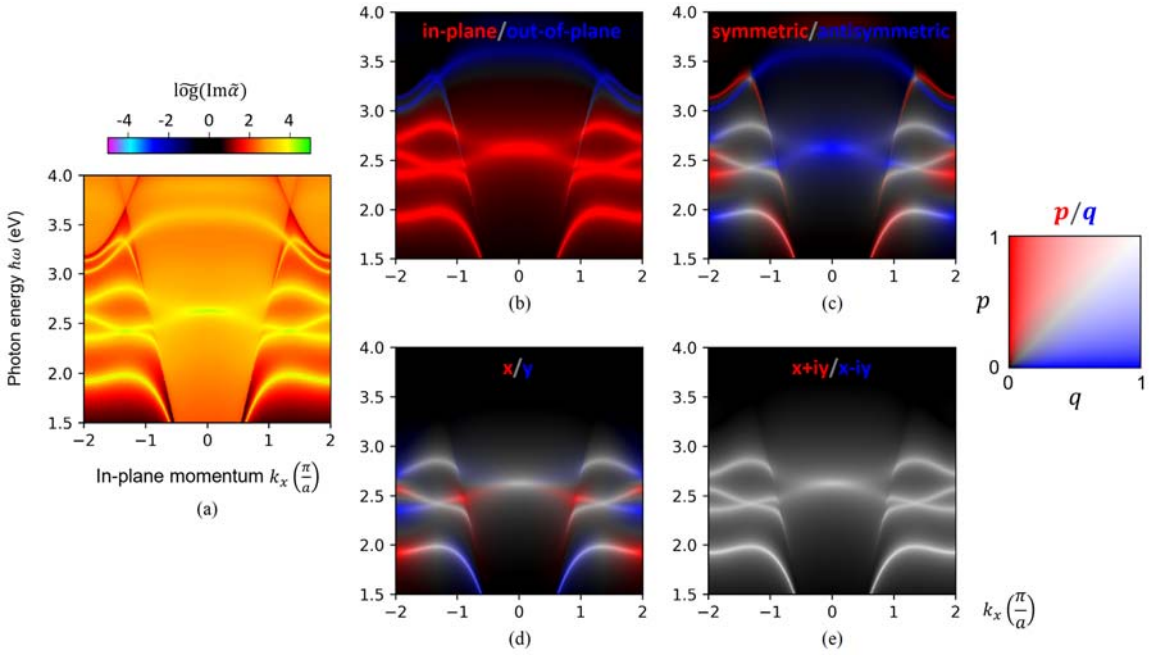

Fig. 6. *Example visualizations of the photonic band structure calculated for the same array as in Figs. 4 and 5, in the spectral range of 1.5–4 eV, and in-plane momentum from −2π/a to 2π/a. (a) Imaginary part of the sum of eigenvalues of the effective lattice polarizability α_{eff}. The color scale (above the plot) corresponds to $\widetilde{\log}\{\mathrm{Im}(\tilde{\alpha})\}$, where $\tilde{\alpha} = 4\pi k a \sum_j \alpha_j / V$, and the function $\widetilde{\log}$ is used to express both positive and negative values in logarithmic scale (see Appendix V). However, in this case, all values are positive. Four subsequent plots present the relative magnitudes of the induced dipole moments p and q encoded in the red/blue color scale defined on the top right (see Appendix V for more details on the color channels). In each case, the dipole moments are induced by two complementary driving fields. White color means equal magnitude of both dipoles, while the overall brightness represents their absolute magnitude. Subsequent plots visualize the separation of bands into (b) in-plane versus out-of-plane, (c) symmetric/antisymmetric, and polarization in the in-plane subspace: (d) linear x/y and (e) circular left/right.*

We will apply this with $\mathbf{A}$ the effective unit cell polarizability, and $\mathbf{v}$ spanning an analysis basis of interest. If one considers as operator a polarizability, then each term $\langle \mathbf{v}_i | \mathbf{A}^\dagger \mathbf{A} | \mathbf{v}_i \rangle$ can physically be interpreted as the magnitude of the total dipole moment induced in the unit cell if one were to apply $\mathbf{v}_i$ as a field to drive it. This norm then allows comparing in how far the operator overlaps with any particular characteristic of interest definable by a space $\mathcal{V}_1$ versus in how far it overlaps with $\mathcal{V}_2$, simply by comparing $||\mathbf{A}||_{\mathcal{V}_1}$ to $||\mathbf{A}||_{\mathcal{V}_2}$.

As example, Fig. 6 reports the band structure defined in $\boldsymbol{\alpha}_{\mathrm{eff}}$ for the same lattice as shown in Figs. 4 and 5 (honeycomb lattice and silver ellipsoids) with (a) simply reporting the effective polarizability without any subspace projection. For this particular geometry, with particles that have no magnetic polarizability and with mirror symmetry in the particle plane, one can immediately project on the electric-only subspace, and furthermore, one expects a separation between in-plane polarized modes and out-of-plane polarized modes. Indeed, upon projection on the appropriate subspaces, performed in (b), one finds a clear separation into modes polarized transverse to the plane and in-plane polarized modes. Note that here to obtain, e.g., the out-of-plane modes one projects on the 2-D subspace consisting of the vectors $\mathbf{v}_1 = (0, 0, 1, 0, \ldots 0)^T$ and $\mathbf{v}_2 = (0 \ldots 0, 1, 0, 0, 0)^T$ polarized along z on particle 1 (sublattice A), respectively, particle 2 (sublattice B), including the magnetic field components in $\mathbf{v}$ in notation for consistency. In Fig. 6(b), red bands correspond to the in-plane polarized subspace norm (red color channel for plotting set by $||\mathbf{A}||_{\mathcal{V}_{\text{in-plane}}}$), whereas blue bands are out-of-plane polarized. For our particular example, due to the particular shape and orientation of the nanoparticles, in-plane and out-of-plane modes are clearly separated in frequency, and in-plane modes appear as dominant at $\hbar\omega < 3$ eV.

In a similar vein, one can project on distinct symmetries within the unit cell, for instance, determining whether the dipole moments $\mathbf{P}_{\mathrm{A}}$ and $\mathbf{P}_{\mathrm{B}}$ on sublattices A and B of an eigenmode will be mainly aligned or antialigned, similar to the projection of "tight-binding" band structures in solid-state physics of electrons onto its orbital contributions. It is well known from the theory of electron and phonon bands in solids, that if a lattice has symmetries in addition to just translation invariance over the periodic lattice vectors (point group symmetries of the unit cell), this imposes additional symmetry constraints on the periodic part of the Bloch wave function [112]–[114]. Therefore, in a solid-state band structure problem where the Bloch wave function reads $\psi_{n,\mathbf{k}}(\mathbf{r}) = u_{n,\mathbf{k}}(\mathbf{r}) e^{i\mathbf{k}\cdot\mathbf{r}}$, the purely periodic

part $u_{n,\mathbf{k}}(\mathbf{r})$ is often analyzed for additional symmetries leading to symmetry-projected or orbital-projected band structures (phrased in the language of density functional theory). Turning to the case at hand of the out-of-plane modes of a honeycomb lattices, projection of the purely periodic part of the Bloch function is tantamount to projecting onto $\mathbf{v}_1 \pm e^{-i\mathbf{k}_{||}\cdot(\mathbf{r}_\mathrm{B}-\mathbf{r}_\mathrm{A})}\mathbf{v}_2$, where the phase factor ensures that solely the periodic part of the Bloch wave function is selected for analysis. Fig. 6(c) shows such an analysis, generalized to all polarizations. Notably, within the light cone, the antisymmetric modes dominantly appear. This is due to the fact that the antisymmetric modes have the lowest radiation damping, and therefore the most distinct signature. That these modes are not actually easy to excite from the far field that is evident from Fig. 5 where they give rise to the peculiar signature of nearly zero transmission at normal incidence. The symmetric modes instead have significant radiative loss and hence are barely visible as a resonance (quality factor $Q < 5$).

Finally, we note that one can also visualize the linear or circular polarization character of the in-plane polarized modes. To this end, one can define the basis vectors spanning x-polarization [defining $\mathbf{v}_{x,1} = (1, 0, 0, 0, \ldots 0)^T$ and $\mathbf{v}_{x,2} = (0 \ldots 1, 0, 0, 0, 0, 0)^T$], respectively, y-polarization, from which their circularly polarized counterparts follow $(\mathbf{v}_{x,i} \pm i\mathbf{v}_{y,i})$. By way of example, Fig. 6 (d)–(e) shows that for our simple honeycomb lattice, the modes can have a significant linear polarization (linked to the k-slice considered, k_x in this example) but not circular polarization. The above-mentioned method can find more sophisticated applications, by tailoring the basis vectors to the topological invariant or symmetry of interest. Another application is in "unfolding" band structures of deformed, defective, or quasi-periodic lattices. In this case, the effective polarizability tensor calculated for an extended unit cell (hence reduced Brillouin zone) can be projected onto eigenmodes of the unperturbed lattice with original unit cell and original Brillouin zone.

IV. PLASMONIC ARRAYS WITH GAIN AND LOSS

The purpose of this section is to present new results on the optical properties of plasmonic arrays with gain and loss that have so far only been studied in tight-binding approximations. We assess if essential features relating to PT-symmetry and topology that are present in tight-binding actually persist in full electrodynamic modeling and at realizable geometrical and material parameters. We consider a honeycomb lattice with period $a = 150$ nm, embedded in a nondispersive passive dielectric medium of refractive index $n_d = 1.5$. We choose the scatterers to be ellipsoidal core–shell nanoparticles, with silver core (dimensions $18 \times 18 \times 6$ nm) and gain medium shell (outer dimensions $54 \times 54 \times 18$ nm), exactly as analyzed in Fig. 2. The permittivities of silver and gain medium are described by (11) and (12), respectively. For silver, we assume the same parameters as specified in Section II-B, whereas for the gain medium, we choose the electric permittivity (at zero gain) $\varepsilon_{g0} = 4$, central frequency $\hbar\omega_g = 2$ eV, and bandwidth $\hbar\gamma_g = 0.1$ eV (the same as in Fig. 2), while tuning the parameter Q between 0 and 0.2 to have gain levels up to ca. 10 000 cm^{-1}, around the highest experimentally reported gain values [79]–[81]. It should be noted that similar physics may be obtainable in practice in systems with lower gain coefficients, spread out more evenly over the unit cell, as evidenced by the experimental reports on plasmon array lasers at gain coefficients not higher than 100 cm^{-1}.

A. Uniform Gain Distribution

In this section, we consider lattices of nanoparticles that all have identical gain, considering a lattice of core–shell nanoparticles in the limit of zero gain as a passive reference. Since the silver cores are twice smaller compared to the nanoparticles assumed in Section III (volume reduced by factor of 8), their radiative interactions are much weaker, giving rise to lattice resonances with much weaker dispersion. The band structure becomes visible only after zooming into the spectral range of 2 ± 0.15 eV. For the passive systems [top plot in Fig. 7(a)], it is even difficult to tell apart subsequent bands (partially due to the logarithmic color scale) due to the combination of radiative and absorptive broadening. At the same time, the scattering cross sections σ_{scat} of these nanoparticles ($\approx$0.02 μm^2, Fig. 2, top left) are still quite similar to the unit cell surface area, giving rise to clear signatures in reflection/transmission, which are shown in Fig. 7(b) (top row).

Fig. 2 suggests that adding gain to the nanoparticles is expected to boost their scattering response in magnitude, to narrow their resonance, and to change their polarizability in phase, hence strongly affecting the optical properties of the lattice. Indeed, the lattice polarizability shown in Fig. 7(a) and far-field response in Fig. 7(b) (middle and bottom rows in both figures) show considerable differences to the no-gain case. At a gain $g \approx 5100$ cm^{-1}, the imaginary part of effective eigenpolarizabilities becomes negative in the guided lattice resonances [cold colors in Fig. 7(a), middle plot], meaning that gain overcomes the purely absorptive loss. At the same time, the imaginary part of polarizability remains positive inside the light cone, meaning that the gain cannot also overcome the additional radiative losses. Nonetheless, the overall increase in the scattering cross section leads to enhanced signatures in transmission and reflection [middle row in Fig. 7(b)]. At higher gain ($g \approx 6600$ cm^{-1}), the radiative damping is suppressed (Fig. 7(a), bottom plot), leading to very strong amplification of light in transmission and reflection [cold colors in Fig. 7(b), bottom row]. This amplification peaks at singular points which are better visible in Fig. 7(c), which shows selected parts of the previous two figures in magnification. Notably, the reflection and transmission diverge to very large values

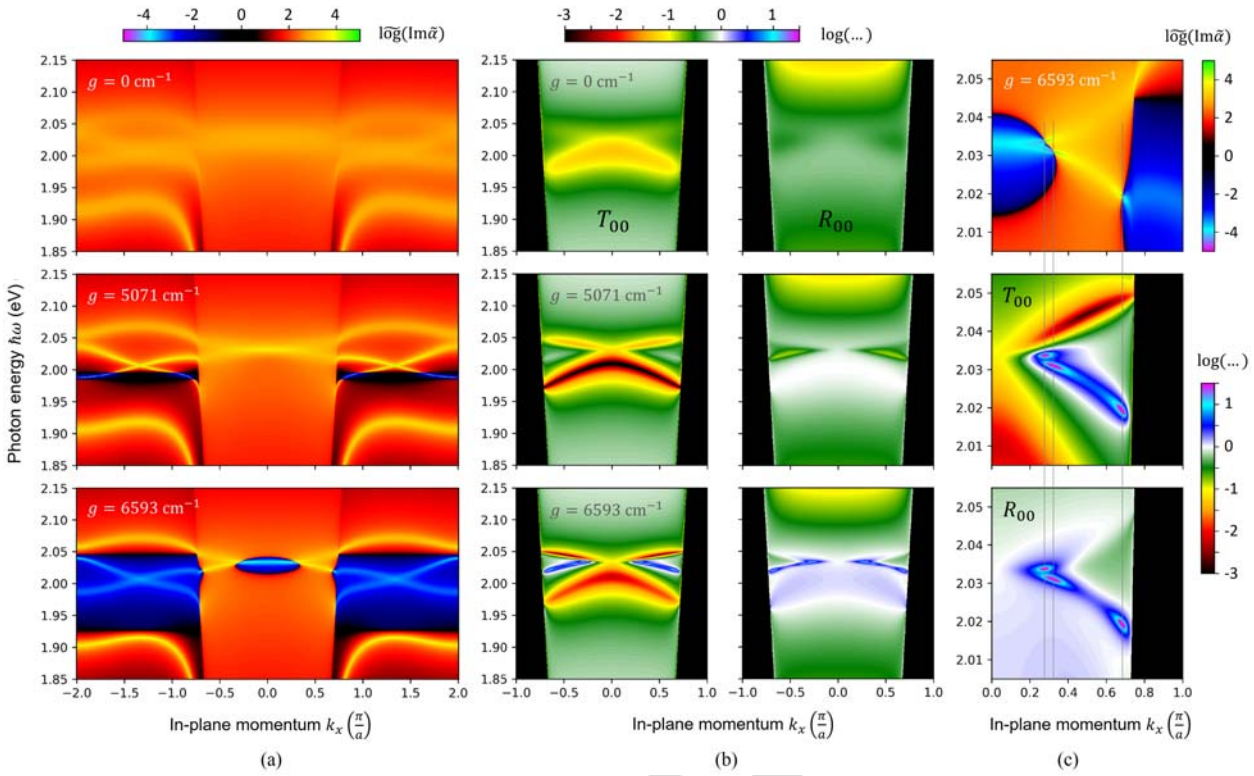

Fig. 7. *Results obtained for the uniform distribution of gain and loss in the lattice. (a) Photonic band structures calculated for the honeycomb lattice (pitch = 150 nm, $n_d = 1.5$) of core–shell ellipsoids (the same as in Fig. 2, with silver core 18 × 18 × 6 nm, and gain medium shell 54 × 54 × 18 nm, $\varepsilon_{g0} = 4$, $\hbar\omega_g = 2$ eV, $\hbar\gamma_g = 0.1$ eV), in the spectral range of 1.85–2.15 eV, and in-plane momentum from $-2\pi/a$ to $2\pi/a$. The gain magnitude Q increases from 0 (top), through 0.1 (middle), up to 0.13 (bottom), giving rise to peak gain coefficients g = 0, 5071, and 6593 cm^{-1}, respectively. The color scale shows $\widetilde{\log}\{\mathrm{Im}(\tilde{\alpha})\}$, where $\tilde{\alpha} = 4\pi ka\sum_j \alpha_j/V$, and $\widetilde{\log}$ is defined in Appendix V. In the first place, adding gain reduces losses, sharpening all resonances, until the losses are completely suppressed and the photonic modes acquire net gain (cold colors). (b) Zero-order transmissivity T_{00} (left column) and reflectivity R_{00} (right column) under illumination by left-handed circularly polarized plane wave, calculated for the same set of parameters as in (a) in-plane momentum from $-\pi/a$ to π/a. Adding gain increases the scattering strength, until both T_{00} and R_{00} exceed unity (cold colors in the bottom row). (c) Points of diverging effective polarizability (top plot), transmissivity (middle), and reflectivity (bottom): magnification of the bottom plot in (a), and of the plots from the bottom row in (b), respectively. Location of singularities is signified by thin vertical lines.*

at conditions where the inverse polarizability $\alpha_{\mathrm{eff}}^{-1}$ crosses zero.

We point out that, in reality, such amplified reflection and transmission can be observed only in the transient response, before the lasing action is established. The amplification will be further limited by gain saturation, by finite size of the array, by spectral and wave vector distribution of incident light, and by finite time duration of the optical pulses. Nevertheless, the above-mentioned constraints are of *technological* rather than *fundamental* nature; hence, one could, in principle, exploit the interplay between material gain and radiation damping at lattice resonances to design a system with arbitrarily large transmission/reflection coefficients. This requires specific conditions that ensure the validity of our linear frequency-domain treatment. In particular, the probe should be significantly weaker in intensity than the pump, such that the gain is not saturated (the response is linear) and the population inversion remains approximately constant over sufficiently long period of time, i.e., comparable to a spontaneous decay rate (justifying the frequency-domain approach).

B. Nonuniform Gain Distribution

Next, we turn to nonidentical scatterers, again considering the honeycomb lattice. The honeycomb lattice allows for two types of scatterers without expanding the unit cell (which would lead to band folding), by putting gain only into the nanoparticles from sublattice B, keeping sublattice A passive. The resulting band structures are shown in Fig. 8(a). Since there is in overall twice less gain in the system, adding $g_{\mathrm{B}} \approx 5100$ cm^{-1} does not compensate the losses, although the lattice resonances become narrower at the Dirac points [band intersections at $|k_x| = 4\pi/(3a)$, top plot in Fig. 8(a)]. Slightly higher gain results in loss compensation and emergence of flat bands with net gain (which is represented by cold colors, as opposed to warm colors corresponding to net loss), separated from lossy bands by sharp singularities (Fig. 8(a), middle plot). At extremely high gain (which is

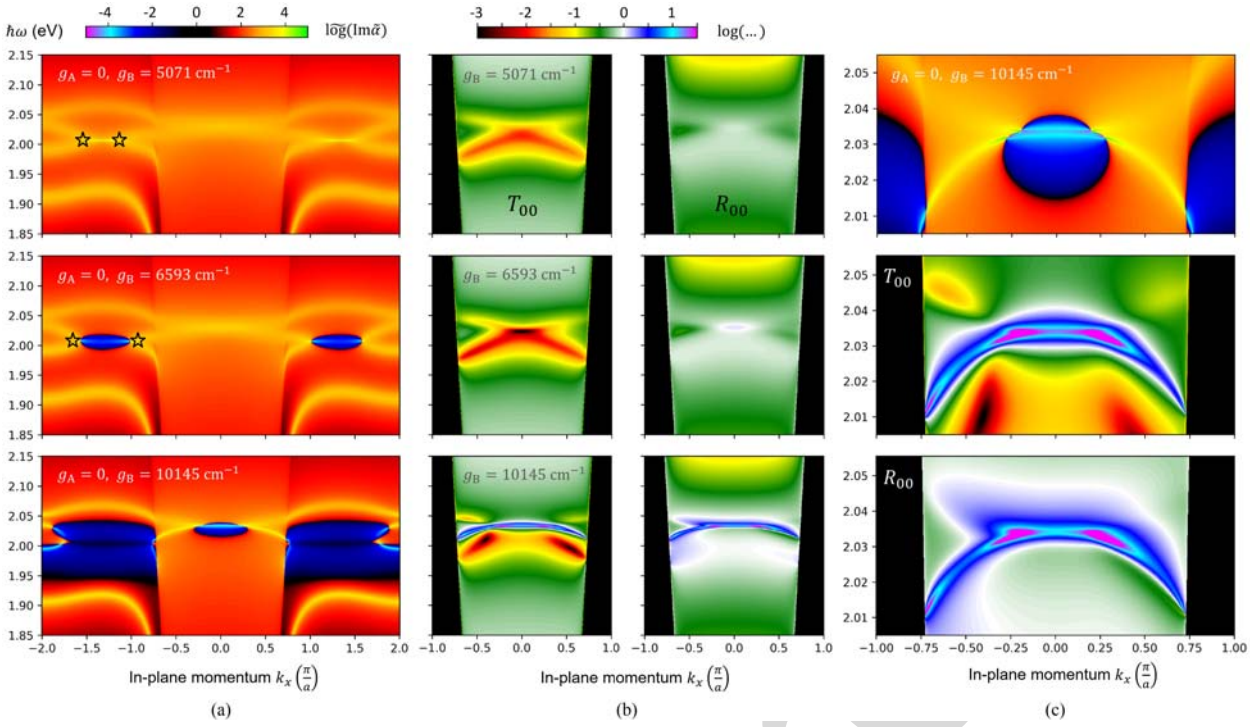

Fig. 8. ***Results obtained for the nonuniform distribution of gain and loss in the lattice. (a) Photonic band structures calculated for the same system as in Fig. 7 (see the caption of Fig. 7 for a detailed description), but with gain only in sublattice B. At moderate gain ($Q_B = 0.1$, top plot), one can observe breaking of PT symmetry around the Dirac points, $|k_x| = 4\pi/(3a)$. At higher gain ($Q_B = 0.13$), the flat bands in the broken-PT phase acquire negative imaginary part, i.e., a net gain. At extremely high gain ($Q_B = 0.2$), the losses are suppressed also within the light cone. Supposed locations of the EPs, where two bands merge but still keep identical damping factors, are marked with stars in the top and middle plots (more details on locating EPs are given in Appendix V). (b) Zero-order transmissivity T_{00} (left column) and reflectivity R_{00} (right column) under left-handed circularly polarized plane wave illumination, calculated for the same set of parameters as in (a). Adding gain only to sublattice B breaks the left-right symmetry in the observables. (c) Magnification of the bottom plot in (a), and of the plots from the bottom row in (b), respectively, showing extreme pseudochiral response due to symmetry breaking in a nonuniform gain-loss metasurface. The color scales are the same as in the corresponding plots in (a) and (b).***

still only present in sublattice B), the radiative losses are also suppressed [Fig. 8(a), bottom plot].

Importantly, a nontrivial reshaping of bands shown in Fig. 8(a) occurs, which is associated with (breaking of) PT symmetry. In the tight-binding model, the honeycomb lattice with alternating gain and loss is well known for the coexistence of PT-unbroken and PT-broken phases across the momentum space [88], [89], [92], [93]. The origin of PT-symmetry breaking in this particular system can be explained as follows. Since the honeycomb lattice is made of two hexagonal sublattices, collective resonances of each sublattice hybridize into twice as many new modes. However, at each Dirac point, the sublattices are effectively decoupled due to the threefold symmetry at the K point of the first Brillouin zone. If the sublattice resonances differ only through gain and loss, but are otherwise identical, the hybridized bands will be degenerate in real eigenfrequencies, but will remain separated in their imaginary eigenfrequencies (this is what we call "broken PT symmetry"). Away from the Dirac points, the situation is opposite (the system is PT-symmetric), so there must be a transition line—a contour of EPs—that borders both regions. At Eps, the two bands have identical real and imaginary eigenvalues and eigenvectors, violating the completeness of the basis set of the underlying non-Hermitian Hamiltonian, which makes them fundamentally intriguing [32]. Fig. 8(a) shows that this physics persists also beyond the tight-binding model. The middle panel clearly shows degeneracy in the real-part of the eigenfrequency (blue flat bands) in a region around the K-points, which only lifts outside the pockets of net gain. The two phases are separated by rings of Eps, which surround the PT-broken phase around each Dirac point. Fig. 8(a) actually only shows a slice through these rings at $k_y = 0$, revealing pairs of EPs (indicated by star-shaped markers). Their full shape spans across k_x-k_y space and can be visualized at a fixed frequency ω (Appendix V).

It is important to distinguish between EPs and the points of diverging polarizability, which we call "singularities," which we already discussed for the case of identical sublattices. Singularities occur where gain overcomes loss, and as Fig. 7(c) shows require neither the coupling between multiple bands, nor the introduction of balanced loss and gain. Conversely, the top plot in Fig. 8(a) has no

singularities and yet there already are EPs around the K-points. Indeed, an EP is defined as coalescence of eigenvalues and eigenvectors of two optical modes and not as a transition from net gain to net loss. In the studied example (and in the great majority of all possible gain–loss metasurfaces), there is no exact balance between gain and loss of any pair of optical modes. At the same time, the imbalance between gain and loss does promote the emergence of singularities in the transition from the PT-broken to PT-unbroken phase. This can be understood by first understanding the origin of net gain in the PT-broken phase. In the exact center of this phase (former Dirac point), the lattice resonances are the same as in two isolated sublattices. Although the losses in sublattice A are larger than the gain in sublattice B, the net extinction of lattice resonance in A can be suppressed by the net gain in B. This is because spectral broadening caused by strong damping effectively reduces the magnitude of the extinction coefficient of the lattice resonance [which is proportional to $\mathrm{Im}(\boldsymbol{\alpha}_{\mathrm{eff}})$]. At the same time, the other mode remains spectrally narrow; hence, its effective amplification is very high, surpassing the extinction of the lossy mode. By contrast, in the PT-unbroken phase, the hybridized modes have net extinction that results from averaging of gain and loss of the two sublattices. The same net extinction is expected at EPs, where both modes coincide in their frequency and in their damping rates. Therefore, the boundary between net extinction and net amplification is expected somewhere along the flat band in the PT-broken phase. The coincidence of resonance with zero net extinction leads to divergent $\boldsymbol{\alpha}_{\mathrm{eff}}$.

C. Polarization Properties

It has been predicted [37] and demonstrated [29] that breaking PT symmetry may lead to observable effects in the polarization properties. In our case, the broken-PT phase is entirely outside the light cone; hence, no significant effects are expected for observables such as lattice reflection and transmission. Nevertheless, the calculated reflectivity and transmissivity under circularly polarized light [Fig. 8(b)] do show an emergent asymmetry between positive and negative values of k_x, an effect known as pseudochirality. While only subtle asymmetry is observed at moderate gain (top and middle rows), it becomes remarkable at extreme gain (bottom row). This is better visible in Fig. 8(c), where one can easily find frequencies at which the reflection and transmission coefficients are $\approx$1 for a given k_x, but nearly diverge at $-k_x$. These observations reflect the potential of gain–loss metasurfaces in exploiting the polarization degree of freedom for tailoring the scattered optical fields.

Within our formalism, also the chirality of modes beyond the light line can be further investigated, following the approach presented in Section III-C using spin-polarized driving fields. Fig. 9 shows the comparison of the relative magnitudes of the dipole moments induced by such driving fields in three different systems. The first system is the honeycomb lattice with uniform gain (considered in the previous section), which shows no differential response to circularly-polarized fields of opposite handedness, as is apparent by lack of colors in the top left plot in Fig. 9. The same balance is evident from the excitation by driving fields focused on either sublattice A or B (top right).

By contrast, the second type of lattice, i.e., the honeycomb lattice with alternating gain and loss [the same as in the middle part of Fig. 8(a) and (b), with gain only in sublattice B] shows remarkably spin-dependent excitation in the broken-PT phase (red and blue colors in the middle-left plot). Similar effects have been previously observed in theoretical studies of PT-symmetric honeycomb photonic crystals [90]. The observed spin dependence of the effective polarizability is reversed at negative momentum. Hence, it can be considered as the analog of pseudochirality for guided lattice resonances. Furthermore, noticeably larger dipole moments are excited in sublattice B compared to sublattice A (middle right), which is associated with the general tendency of light toward localization in regions with gain, one of the basic properties of systems with a broken PT symmetry [115].

The emergent pseudochirality is also observed in "gapped" systems (bottom row in Fig. 9), where the scatterers of two sublattices are mutually detuned by slight modification of their shape (the ellipsoids in sublattice B are slightly more spherical compared to the ellipsoids in sublattice A). Detuning opens a band gap at the Dirac points, giving rise to spin-polarized bands (bottom left). In this case, the pseudochirality at the band edges is associated with an unbalanced contribution of two sublattices, with the blue-detuned sublattice B appearing dominant in the upper band edge (blue "conduction band" in the bottom right plot), and the red-detuned sublattice A taking over the lower band edge (red "valence band"). Detuning of sublattice resonances is a complementary degree of freedom as it modulates the real part of the eigenfrequencies, compared to the gain–loss distribution, which modulates the imaginary part. According to Szameit *et al.* [88], in the tight-binding picture, this has an analogy with particle physics, where the first scenario corresponds to massive Dirac fermions, whereas the second scenario gives rise to tachyons—particles of imaginary mass [88]. Combination of both parameters allows exploring the topology of photonic bands, which is demonstrated in the next section.

D. Topology of Exceptional Points

One can argue that the frequency-wave vector diagrams of lattice polarizability do not allow a precise pinpointing of either the bands or the EPs. A definitive proof of EPs is the coalescence of eigenvectors. However, by the very nature of the description of plasmon arrays with gain and loss in an electrodynamic framework with retardation, eigenfrequencies and hence also eigenmodes are not sharply defined. Indeed, any real-valued wave vector

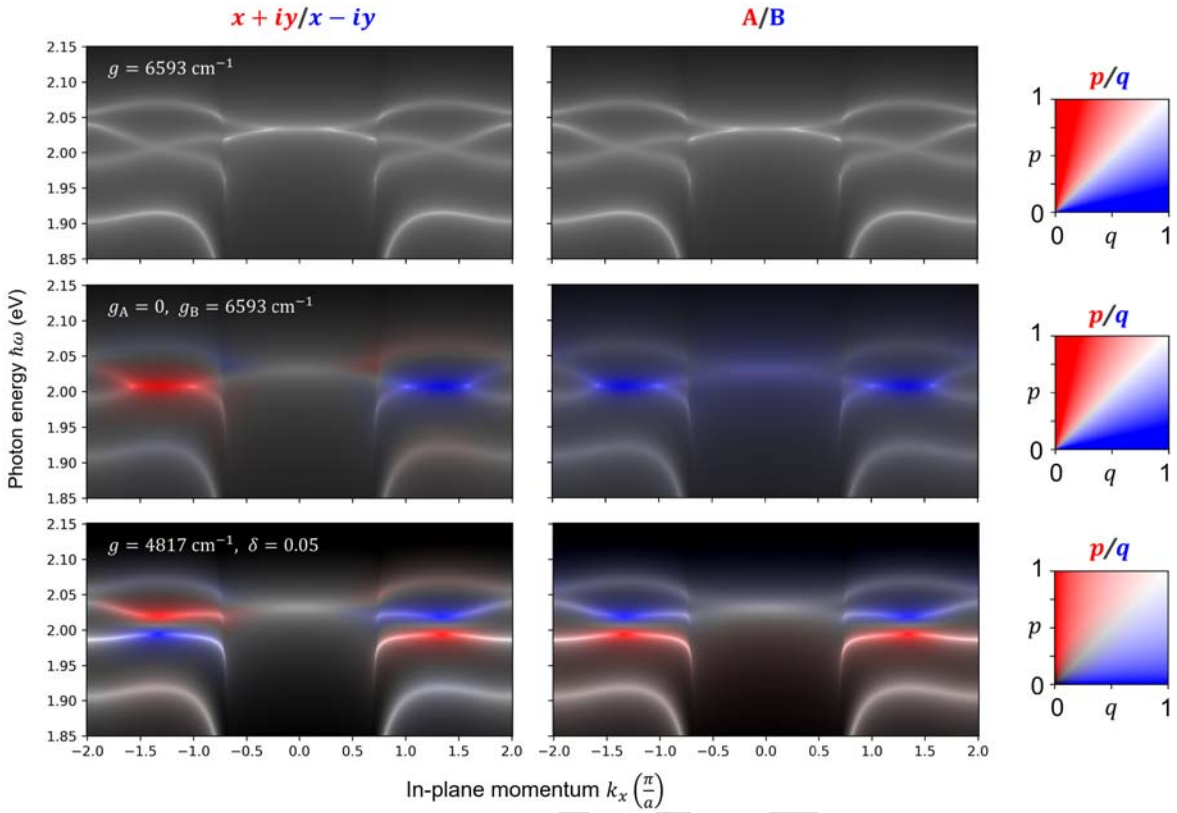

Fig. 9. *Relative contribution of the dipole moments excited by spin-polarized driving fields (left column) and by sublattice-selective driving fields (right column). The first row corresponds to the honeycomb lattice with uniform gain [the same as in the bottom plot in Fig. 7(a)]. The second row shows the results for the honeycomb lattice with gain only in sublattice B [the same as in the middle plot in Fig. 8(a)]. Results presented in the third row are obtained for the honeycomb lattice with uniform but relatively small gain, and with relative detuning of the LSPRs between sublattices A and B, obtained by setting a different aspect ratio of the ellipsoidal nanoparticles in each sublattice: (3+δ):(3+δ):1 in sublattice A, and (3−δ):(3−δ):1 in sublattice B. Details on the color encoding are given in Appendix V.*

real-valued frequency visualization of the dispersion relation will show bands with finite width due to gain and absorption/radiation loss, making the precise tracing of eigenvectors associated with bands cumbersome. We show example results of such a tracking approach in Appendix V. In this section, we instead provide another evidence of EPs, based on the topology of photonic bands.

One of the most fascinating properties of EPs is the topology of eigenvalue surfaces ("Riemann sheets") in their surroundings. In that context, EPs are described by a fractional topological charge ("vorticity") [30]. Calculation of this topological invariant requires encircling of a single EP in the given parameter space [116], e.g., in momentum space, which has been recently demonstrated in periodic scattering systems [29]. Our system does not have isolated EPs, but rings of EPs ("exceptional rings"), surrounding the Dirac points. Hence, it is not possible to extract the topological invariant by traveling only across the 2-D momentum space. Instead, we set $k_y = 0$ and form an appropriate parameter space with k_x as one axis, and as the second degree of freedom, a parameter δ that enables mutual detuning between the LSPRs of sublattices A and B, by deformation. The initial aspect ratio of each nanoparticle is 3:3:1, which is modified by δ into $(3+\delta):(3+\delta):1$ in sublattice A and $(3-\delta):(3-\delta):1$ in sublattice B. This is the type of deformation also used to open the band gap at the Dirac points (Fig. 9, bottom row, $\delta = 0.05$).

Fig. 10 shows the evolution of photonic bands along a closed trajectory in the k_x-δ space. In the first step, we keep k_x away from the Dirac point and tune δ continuously from negative to positive. In the second step, δ is fixed and k_x is tuned closer to the Dirac point (but still at some distance from it). Next, δ is changed back from positive to negative, and finally, k_x is moved back to the previous value, which closes the loop.

For the honeycomb lattice with uniform gain, the ordering of photonic bands along the frequency axis does not change at any point of the trajectory and remains the same after completing the entire loop (Fig. 10, top). By contrast, in the gain–loss honeycomb (Fig. 10, bottom), one of the bands clearly makes it all the way to the resonant frequency of another mode and vice versa. As a result, the two bands are interchanged after completing the loop, showing a nontrivial topology identical to the Möbius strip. In other words, if we decide to trace one of these bands,

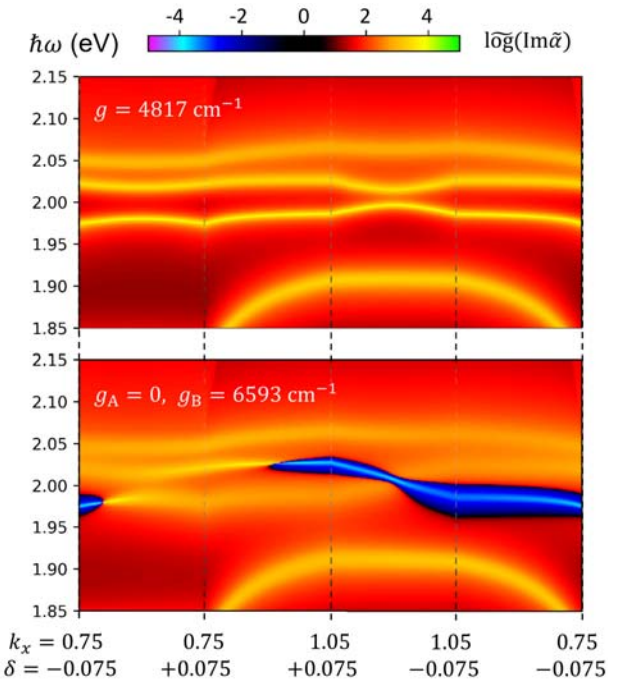

Fig. 10. *Evolution of the effective polarizability across two parameters: in-plane momentum k_x (π/a), and detuning δ. The horizontal axis corresponds to a closed loop in this parameter space. The top plot shows the photonic bands of the honeycomb lattice with uniform gain, whereas the bottom plot corresponds to the lattice with alternating gain-loss pattern. In the top plot, the bands do not cross at any point, meaning that there is no EP inside the loop. By contrast, in the bottom plot, two bands interchange, showing nontrivial topology typical for the surrounding of an EP.*

we would have to complete the loop twice in order to end up at the same frequency. This kind of topology is typical for the direct vicinity of EPs, suggesting that at least one EP has been encircled by the selected trajectory. This final example demonstrates that gain and loss in periodic arrays can have highly counter-intuitive consequences, going far beyond simple amplification or extinction of light. Moreover, the results presented in Fig. 10 constitute a strong evidence that the topological features predicted by the tight-binding model persist in the nanoparticle arrays even in the presence of retardation and radiative damping. Here, this remarkable fact is demonstrated for a non-Hermitian system hosting PT-symmetric and PT-broken phases separated by EPs, which complements similar findings in plasmonic realizations of the Su–Schrieffer–Heeger model [117].

V. CONCLUSION

The passing decade has seen a rapid development of two research fields: on the one hand, large progress has been made in the field of metasurface lasers based on plasmonic nanoparticle arrays combined with gain media [3]; on the other hand, significant research efforts have been invested in the field of non-Hermitian photonics [6], [7], where gain and loss give rise to nontrivial effects associated with PT symmetry. Surprisingly, the overlap between these two fields has been almost negligible, despite the fact that the nanostructured plasmonic and active materials could offer an excellent platform for engineering the spatial distribution of gain and loss, enabling the realization of a variety of non-Hermitian models, especially those associated with collective resonances of periodic lattices [31], [32]. One of the factors that hinder the emergence of *non-Hermitian plasmonics* is the "broken PT symmetry" of the available materials. In other words, plasmonic losses are typically many orders of magnitude larger than the material gain. However, materials science continuously moves forward [79], promising gain coefficients capable of compensating the losses of plasmonic metals, which could bring the field of PT-symmetric plasmonic arrays into fruition.

In this article, we have presented a minimal but rigorous theoretical framework that can be used for modeling of periodic lattices of optical dipolar nanoscatterers with gain and loss. This article provides a self-consisted toolbox that is suitable for quantitative evaluation of observable optical properties: reflection, transmission, diffraction, resolved in frequency, momentum, phase, and polarization, as well as symmetry, dispersion, and net extinction/amplification of guided lattice resonances. The presented method is suitable for studies on complicated 2-D arrays, with many scatterers of arbitrary 3-D arrangement within the unit cell, each scatterer possessing its own resonant frequency, anisotropic, or bianisotropic optical response, and gain/loss properties. We believe that the presented theoretical approach could be useful in designing optical metasurfaces of desired functions, including PT-symmetric plasmonic lattices suitable for lasing, wavefront shaping, optical computing [118], or solving fundamental scientific problems, such as breaking the fundamental limits of passive optical elements [5], [119] and emulation of various non-Hermitian models [88], [92]. As an example, we have demonstrated here the capability of this method to investigate breaking of PT symmetry at the Dirac points of guided lattice resonances in the gain/loss honeycomb lattice, showing the emergence of EPs and their nontrivial Möbius strip topology, as well as the presence of spin-polarized flat bands with net gain and inevitable catastrophic singularities associated with divergence of effective polarizability at the points where the flat lattice resonances coincide with conditions of perfectly balanced gain and loss. Extension of this model to active magnetoelectric, nonlinear, nonreciprocal, and time-dependent (Floquet) metasurfaces [120], [121] is an exciting avenue of future research. Furthermore, we note that the model is easily extendable to lattices integrated in arbitrary stratified systems by modification of the Green function, and to dealing with other excitations and observables than those associated with plane waves, for instance, using the array scanning method to gain insight into the LDOSs experienced by point sources placed in the system [122].

On the other hand, extending our theoretical framework to the regime of transient gain dynamics and lasing calls for further developments. In particular, the coupled-wave theory that is commonly used to describe distributed feedback lasing in periodic nanoparticle arrays has recently been shown to fail in terms of quantitative matching with the band structure parameters [123]. Resolving this issue requires a real-space model, especially in finite-sized and hierarchical systems [28], [124], replacing the reciprocal-space description based on the plane wave approximation. Addressing these issues would enable accurate design of non-Hermitian metasurface lasers and active light-shaping devices.

APPENDIX A
SYSTEM OF UNITS USED IN THIS ARTICLE

The system of units used in our work is the same as in [54]. This system of units is different from the Gaussian (CGS) system, although it offers similar benefits. In our system, the amplitudes of electric and magnetic fields of a plane wave are identical, i.e., $|\mathbf{E}| = |\mathbf{H}|$, regardless of the dielectric background, and moreover, the intensity of a plane wave can be expressed as: $I = |\mathbf{E}|^2/(2Z) = |\mathbf{H}|^2/(2Z)$. By comparison, in the Gaussian system, $|\mathbf{E}|$ and $|\mathbf{H}|$ are of similar order of magnitude but differ by wave impedance. Conversion from SI units to the system of units used in our work is presented in Table 1. Conversion factors given in Table 1 involve the wave impedance Z of the background medium, its electric permittivity ε, and the velocity of light c.

Table 1 System of Units Used in This Article

Eq.	Symbol	Quantity	Conversion from SI
(2)	$\mathbf{E}$	electric field	$\mathbf{E}^{(\mathrm{SI})}$
(2)	$\mathbf{H}$	magnetic field	$Z\,\mathbf{H}^{(\mathrm{SI})}$
(2)	$\mathbf{p}$	electric dipole moment	$\frac{1}{4\pi\varepsilon}\mathbf{p}^{(\mathrm{SI})}$
(2)	$\mathbf{m}$	magnetic dipole moment	$\frac{Z}{4\pi}\mathbf{m}^{(\mathrm{SI})}$
(3)	$\boldsymbol{\alpha}_{EE}$	electric polarizability	$\frac{1}{4\pi\varepsilon}\boldsymbol{\alpha}^{(\mathrm{SI})}_{EE}$
(3)	$\boldsymbol{\alpha}_{HH}$	magnetic polarizability	$\frac{1}{4\pi}\boldsymbol{\alpha}^{(\mathrm{SI})}_{HH}$
(3)	$\boldsymbol{\alpha}_{EH}$	electric-magnetic polarizability	$\frac{c}{4\pi}\boldsymbol{\alpha}^{(\mathrm{SI})}_{EH}$
(3)	$\boldsymbol{\alpha}_{HE}$	magnetic-electric polarizability	$\frac{Z}{4\pi}\boldsymbol{\alpha}^{(\mathrm{SI})}_{HE}$
(15)	$\mathbf{G}^0_{EE}$	electric Green function	$4\pi\varepsilon\,\mathbf{G}^{0\,(\mathrm{SI})}_{EE}$
(15)	$\mathbf{G}^0_{HH}$	magnetic Green function	$4\pi\,\mathbf{G}^{0\,(\mathrm{SI})}_{HH}$
(15)	$\mathbf{G}^0_{EH}$	electric-magnetic Green function	$\frac{4\pi}{Z}\mathbf{G}^{0\,(\mathrm{SI})}_{EH}$
(15)	$\mathbf{G}^0_{HE}$	magnetic-electric Green function	$\frac{4\pi}{c}\mathbf{G}^{0\,(\mathrm{SI})}_{HE}$

APPENDIX B
ELLIPSOIDAL AND CORE-SHELL NANOPARTICLES

Consider ellipsoidal nanoparticles of permittivity ε_2 embedded in a medium of permittivity ε_1, with symmetry axes oriented along the Cartesian axes. Generalization of (9) can be written as [62]

$$\boldsymbol{\alpha}_{\mathrm{stat},EE} = V \begin{pmatrix} A_x \\ A_y \\ A_z \end{pmatrix} \mathbb{I}_{3\times 3} \tag{41}$$

where A_j are separately defined for each symmetry axis $j = x, y, z$ as a function of the corresponding shape factor L_j

$$A_j = \frac{\varepsilon_2 - \varepsilon_1}{L_j\,(\varepsilon_2 - \varepsilon_1) + \varepsilon_1}. \tag{42}$$

Shape factors are expressed in terms of the subsequent radii r_j of the ellipsoid

$$L_j = \frac{r_x r_y r_z}{2} \int_0^\infty \frac{ds}{(s+r_j^2)\sqrt{(s+r_x^2)(s+r_y^2)(s+r_z^2)}} \tag{43}$$

where L_j are constrained by condition $L_x + L_y + L_z = 1$, which immediately gives the value of L_j for the sphere: $L_x = L_y = L_z = 1/3$, and reduces (41)–(43) to (9).

Ellipsoidal core–shell nanoparticles with core permittivity ε_3 and shell permittivity ε_2, embedded in a medium of permittivity ε_1 [65], can be described by the same formula as (41) with A_j governed by

$$A_j = \frac{B_j^{-1} - \beta C_j^{-1}}{(B_j D_j)^{-1} + \beta L_{2,j}\,(1 - L_{2,j})} \tag{44}$$

where β is the volume fraction of the core, and B_j, C_j, and D_j are defined as

$$\begin{aligned} B_j &= \frac{\varepsilon_3 - \varepsilon_2}{L_{3,j}\,(\varepsilon_3 - \varepsilon_2) + \varepsilon_2} \\ C_j &= \frac{\varepsilon_1 - \varepsilon_2}{L_{2,j}\,(\varepsilon_1 - \varepsilon_2) + \varepsilon_2} \\ D_j &= \frac{\varepsilon_2 - \varepsilon_1}{L_{2,j}\,(\varepsilon_2 - \varepsilon_1) + \varepsilon_1} \end{aligned} \tag{45}$$

where $L_{3,j}$ and $L_{2,j}$ are the shape factors of the core and shell, respectively. For spherical core–shell nanoparticles, (41)–(45) can be reduced to

$$\boldsymbol{\alpha}_{\mathrm{stat},EE} = 3V \frac{B^{-1} - \beta C^{-1}}{(BC)^{-1} + 2\beta} \mathbb{I}_{3\times 3} \tag{46}$$

where

$$B = \frac{\varepsilon_3 - \varepsilon_2}{\varepsilon_3 + 2\varepsilon_2} \quad C = \frac{\varepsilon_1 - \varepsilon_2}{\varepsilon_1 + 2\varepsilon_2} \quad D = \frac{\varepsilon_2 - \varepsilon_1}{\varepsilon_2 + 2\varepsilon_1}. \tag{47}$$

APPENDIX C
DYADIC LATTICE SUM

The goal of this appendix is to provide pointers on how to efficiently calculate the lattice sums $\mathcal{G}$ and $\mathcal{G}^{\neq}$ from (19) and (20). For this purpose, we first consider the lattice sum that involves the scalar version of the Green function from (15). This sum is poorly convergent, however, following the technique developed by Ewald [40] and Jordan *et al.* [41], it can be decomposed into the reciprocal- and real-space summations $\Gamma^{(1)}$ and $\Gamma^{(2)}$, each converging exponentially

$$\sum_{m,n} \frac{e^{ik|\mathbf{R}_{m,n}-\mathbf{r}|}}{|\mathbf{R}_{m,n}-\mathbf{r}|} e^{i\mathbf{k}\cdot\mathbf{R}_{m,n}} = \Gamma^{(1)} + \Gamma^{(2)}. \tag{48}$$

The reciprocal-space summation reads

$$\Gamma^{(1)} = \frac{\pi}{S} \sum_{\tilde{m},\tilde{n}} e^{ik(\tilde{x},\tilde{y})^T\cdot\mathbf{r}_{||}} f^{(1)}_{\tilde{m},\tilde{n}}(z) \tag{49}$$

where $k(\tilde{x},\tilde{y})^T = \mathbf{k}_{||} + \mathbf{K}_{\tilde{m},\tilde{n}}$ is the in-plane component of the diffracted wave vector [see (32) and (33)]. The real-space summation is expressed as

$$\Gamma^{(2)} = \sum_{m,n} e^{i\mathbf{k}_{||}\cdot\mathbf{R}_{m,n}} f^{(2)}(\rho_{m,n}) \tag{50}$$

where $\mathbf{r} = (\mathbf{r}_{||}, z)^T$ are the real-space coordinates and $\rho_{m,n} = |\mathbf{R}_{m,n} - \mathbf{r}|$. The functions $f^{(1)}_{\tilde{m},\tilde{n}}(z)$ and $f^{(2)}(\rho_{m,n})$ are defined as

$$f^{(1)}_{\tilde{m},\tilde{n}}(z) = \frac{F(k\tilde{z}, |z|) + F(k\tilde{z}, -|z|)}{k\tilde{z}} \tag{51}$$

$$f^{(2)}(\rho_{m,n}) = \frac{F(ik, \rho_{m,n}) + F(-ik, \rho_{m,n})}{2\rho_{m,n}} \tag{52}$$

where $k\tilde{z} = \sqrt{k^2 - |\mathbf{k}_{||} + \mathbf{K}_{\tilde{m},\tilde{n}}|^2}$ is the out-of-plane component of the diffracted wave vector, and the function $F(p,q)$ has the form

$$F(p,q) = e^{ipq}\,\mathrm{erfc}\left(\frac{p}{2\eta} + q\eta\right) \tag{53}$$

where $\mathrm{erfc}(\ldots)$ is the complex error function. The parameter η should be chosen around $\sqrt{\pi}/a$ for optimal convergence (where a is the lattice period). The summation cutoff should be chosen depending on the number of nonevanescent diffracted orders; however, for dense lattices ($a \leqslant 2\pi/k$), good convergence is achieved [44], [45] already with $|m,n| \leqslant 5$.

The dyadic lattice sum is generated by applying the differential operator from (15) to each summand in (49) and (50). The reciprocal-space sum $\Gamma^{(1)}$ depends only on the radius $|\mathbf{r}_{||}|$ and height z in cylindrical coordinates, which yields the following formulas:

$$\begin{aligned}(\mathbb{I}_{3\times3}k^2 + \nabla\otimes\nabla)e^{ik(\tilde{x},\tilde{y})^T\cdot\mathbf{r}_{||}} f^{(1)}_{\tilde{m},\tilde{n}}(z) \\ = e^{ik(\tilde{x},\tilde{y})^T\cdot\mathbf{r}_{||}} \\ \times \left[\begin{pmatrix} 1-\tilde{x}^2 & -\tilde{x}\tilde{y} & 0 \\ -\tilde{x}\tilde{y} & 1-\tilde{y}^2 & 0 \\ 0 & 0 & 1\end{pmatrix} k^2 \right. \\ \left. + \begin{pmatrix} 0 & 0 & i\tilde{x} \\ 0 & 0 & i\tilde{y} \\ i\tilde{x} & i\tilde{y} & 0\end{pmatrix} k\frac{d}{dz} + \begin{pmatrix} 0 & 0 & 0 \\ 0 & 0 & 0 \\ 0 & 0 & 1\end{pmatrix} \frac{d^2}{dz^2}\right] f^{(1)}_{\tilde{m},\tilde{n}}(z)\end{aligned} \tag{54}$$

for the diagonal blocks, and

$$\begin{aligned}-ik\nabla\times e^{ik(\tilde{x},\tilde{y})^T\cdot\mathbf{r}_{||}} f^{(1)}_{\tilde{m},\tilde{n}}(z) = ke^{ik(\tilde{x},\tilde{y})^T\cdot\mathbf{r}_{||}} \\ \times \left[\begin{pmatrix} 0 & 0 & -\tilde{y} \\ 0 & 0 & \tilde{x} \\ \tilde{y} & -\tilde{x} & 0\end{pmatrix} + \begin{pmatrix} 0 & i & 0 \\ -i & 0 & 0 \\ 0 & 0 & 0\end{pmatrix} \frac{d}{dz}\right] f^{(1)}_{\tilde{m},\tilde{n}}(z)\end{aligned} \tag{55}$$

for the off-diagonal blocks, respectively. At the same time, $\Gamma^{(2)}$ depends only on radius $r = |\mathbf{r}|$ in spherical coordinates, which leads to the following formulas:

$$\begin{aligned}(\mathbb{I}_{3\times3}k^2 + \nabla\otimes\nabla) f^{(2)}(\rho_{m,n}(r)) \\ = \left[\mathbb{I}_{3\times3}\left(k^2 + \frac{1}{r}\frac{d}{dr}\right)\right. \\ \left. + \begin{pmatrix} x^2 & xy & xz \\ xy & y^2 & yz \\ xz & yz & z^2\end{pmatrix} \frac{1}{r}\frac{d}{dr}\frac{1}{r}\frac{d}{dr}\right] f^{(2)}(\rho_{m,n}(r))\end{aligned} \tag{56}$$

for the diagonal blocks, and

$$\begin{aligned}-ik\nabla\times f^{(2)}(\rho_{m,n}(r)) \\ = \begin{pmatrix} 0 & z & -y \\ -z & 0 & x \\ y & -x & 0\end{pmatrix} \frac{ik}{r}\frac{d}{dr} f^{(2)}(\rho_{m,n}(r))\end{aligned} \tag{57}$$

for the off-diagonal blocks. Applying all the above-mentioned derivatives allows obtaining the dyadic lattice sum $\mathcal{G}$ in (27). However, the calculation of $\mathcal{G}^{\neq}$ requires extra attention, as the simple omission of the zero-order term ($m = 0, n = 0$) in the Ewald sum [left-hand side of (48)] is not straightforward. Instead, one can first calculate $\mathcal{G}$ by performing the full summation and then subtract the dyadic Green tensor $\mathbf{G}^0$ of the homogeneous dielectric medium, calculated directly by (15), setting $\mathbf{r} = \mathbf{r}_{\text{off}}$

and $\mathbf{r}' = \mathbf{R}_{0,0}$

$$\mathcal{G}^{\neq} = \mathcal{G} - \mathbf{G}^0(\mathbf{r}_{\text{off}} - \mathbf{R}_{0,0}). \tag{58}$$

The problem arises because $\mathbf{G}^0$ is singular if the observation point is located exactly at the lattice origin, i.e., $\mathbf{r}_{\text{off}} = \mathbf{R}_{0,0}$. One way to resolve this problem is to evaluate two (or more) tensors at some finite (but small) symmetric offsets $\mathbf{r}_{\text{off}}$ from the lattice origin, e.g., along $+z$ and $-z$, and then taking the arithmetic average of these tensors.

APPENDIX D
MODIFIED LOG FUNCTION

The function $\widetilde{\log}$ is a modified decimal logarithm that allows to display both positive and negative values. It is defined as

$$\widetilde{\log}(\xi) = \operatorname{sgn}(\xi)\frac{\log|\xi| + |\log|\xi||}{2}. \tag{59}$$

The above function truncates all values ξ that fall into $|\xi| < 1$ (at $\log|\xi| = 0$), and therefore, it is suitable for plotting positive and negative values spanning several orders of magnitude, from any range symmetric around zero, e.g., from -10^5 to 10^5. In this article, we use $\widetilde{\log}$ to plot the sum of imaginary parts of effective eigenpolarizabilities: $\widetilde{\log}(\operatorname{Im}\tilde{\alpha}_{\text{eff}})$, where

$$\tilde{\alpha}_{\text{eff}} = \frac{4\pi k a}{V}\sum_j \alpha_{\text{eff},j} \tag{60}$$

where V is the volume of the nanoscatterers, k is the wavenumber (in the embedding dielectric medium), a is the lattice period, and j is the eigenvalue index.

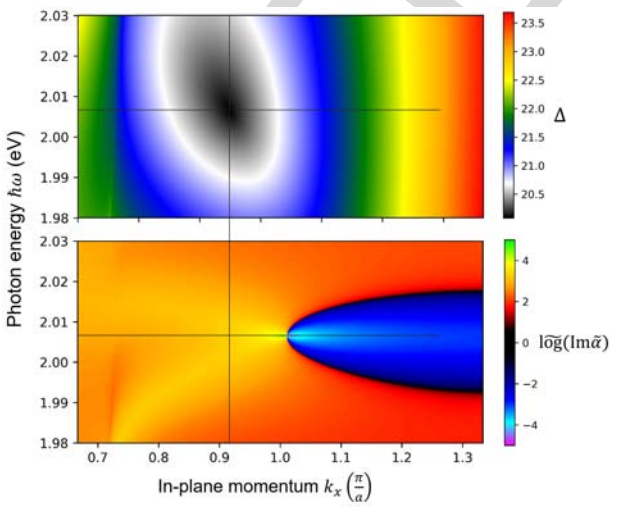

Fig. 11. *Coallescence of eigenvectors quantified by Δ (63) (top) and compared to the imaginary eigenpolarizability (bottom).*

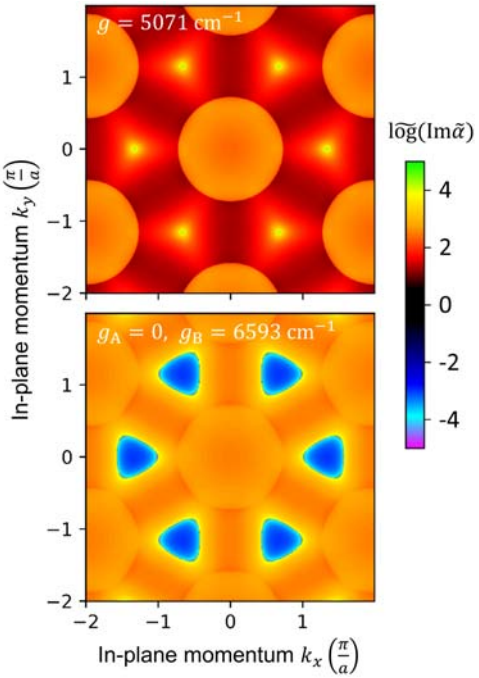

Fig. 12. *Fixed-frequency slices ($\hbar\omega = 2.0065$ eV) of the band structures presented in Fig. 7(a)-middle and Fig. 8(a)-middle (top and bottom, respectively), showing the momentum-space extent of the net gain in the PT-broken phase around all six Dirac points.*

APPENDIX E
RGB COLOR ENCODING

Four plots in Fig. 6(b)–(e) and plots in Fig. 9 display two types of information: the overall intensity and the relative content of two values (p and q). The first information is contained in the brightness, whereas the second information is encoded in the interplay between red and blue colors. Shades of red indicate a dominant contribution of p, whereas shades of blue are associated with superior values of q. White color means a balanced contribution of p and q. The above-mentioned encoding is based on the customized RGB content

$$\begin{aligned} \mathrm{R} &= \operatorname{trun}\{\mathrm{R'}[1 + \mathrm{S}(\mathrm{R'} - \mathrm{B'})]\} \\ \mathrm{B} &= \operatorname{trun}\{\mathrm{B'}[1 - \mathrm{S}(\mathrm{R'} + \mathrm{B'})]\} \\ \mathrm{G} &= \min\{\mathrm{R}, \mathrm{B}\} \end{aligned} \tag{61}$$

where S is a parameter responsible for color saturation, and "trun" denotes the truncation to the range between 0 and 1 (all values greater than 1 are set to 1, whereas all values smaller than 0 are set to 0). Colors are further enhanced by applying the following functions:

$$\begin{aligned} \mathrm{R'} &= \operatorname{trun}\left\{1 + \frac{\mathrm{C}}{2}\log\left[\frac{p}{\max(p_{\max}, q_{\max})}\right]\right\} \\ \mathrm{B'} &= \operatorname{trun}\left\{1 + \frac{\mathrm{C}}{2}\log\left[\frac{q}{\max(p_{\max}, q_{\max})}\right]\right\} \end{aligned} \tag{62}$$

where C is a parameter responsible for contrast, and $p_{\max}$, $q_{\max}$ are the maximum values in the investigated k-ω range. Both S and C can be chosen 1 by default and then customized depending on the range of p and q values.

APPENDIX F
COALESCENCE OF EIGENSTATES

We attempt to locate EPs by calculating the sum of differences between all possible pairs of eigenvectors $\mathbf{v}_j$ obtained by diagonalization of $\boldsymbol{\alpha}_{\text{eff}}$

$$\Delta = \sum_{ij} |\mathbf{v}_i - \mathbf{v}_j|^2. \tag{63}$$

Fig. 11 shows Δ (top) compared to $\mathrm{Im}(\tilde{\alpha})$ (zoom-in view in in Fig. 10, middle). As we can see, Δ has a minimum that is slightly shifted along the momentum axis compared to the position of the singularity. The value at this minimum is far from zero due to the mixing of eigenvectors from multiple pairs, most of which do not participate in the formation of EP.

APPENDIX G
PT-BROKEN PHASE IN THE K-SPACE

Breaking PT-symmetry in the honeycomb lattice creates a ring of EPs at each Dirac point in the Brillouin zone [88], [93]. Band structures in Fig. 8 show only a "side view" of two such regions with PT-broken phase. Here, for completeness, we show k_x–k_y map of these regions at a fixed frequency corresponding to the spectral position of Dirac degeneracies. Fig. 12 (top) shows the Dirac points in the honeycomb lattice with uniform gain distribution, whereas Fig. 12 (bottom) plot shows the same k-space region at exactly the same frequency for the alternating gain/loss pattern. The "shape" of the boundaries surrounding the PT-broken net-gain regions turns out to be similar to rounded triangles rather than perfectly circular. ■

Acknowledgments

The authors would like to thank K. Cognée for useful discussion on exceptional points.

REFERENCES

[1] V. G. Kravets, A. V. Kabashin, W. L. Barnes, and A. N. Grigorenko, "Plasmonic surface lattice resonances: A review of properties and applications," *Chem. Rev.*, vol. 118, no. 12, pp. 5912–5951, Jun. 2018.
[2] W. Wang, M. Ramezani, A. I. Väkeväinen, P. Törmä, J. G. Rivas, and T. W. Odom, "The rich photonic world of plasmonic nanoparticle arrays," *Mater. Today*, vol. 21, no. 3, pp. 303–314, 2018.
[3] D. Wang, W. Wang, M. P. Knudson, G. C. Schatz, and T. W. Odom, "Structural engineering in plasmon nanolasers," *Chem. Rev.*, vol. 118, pp. 2865–2881, Oct. 2018.
[4] N. Meinzer, W. L. Barnes, and I. R. Hooper, "Plasmonic meta-atoms and metasurfaces," *Nature Photon.*, vol. 8, no. 12, pp. 889–898, Dec. 2014.
[5] N. M. Estakhri and A. Alù, "Wave-front transformation with gradient metasurfaces," *Phys. Rev. X*, vol. 6, no. 4, 2016, Art. no. 041008.
[6] L. Feng, R. El-Ganainy, and L. Ge, "Non-Hermitian photonics based on parity–time symmetry," *Nature Photon.*, vol. 11, pp. 752–762, Dec. 2017.
[7] M. A. Miri and A. Alù, "Exceptional points in optics and photonics," *Science*, vol. 363, no. 6422, p. eaar7709, 2019.
[8] S. Zou, N. Janel, and G. C. Schatz, "Silver nanoparticle array structures that produce remarkably narrow plasmon lineshapes," *J. Chem. Phys.*, vol. 120, no. 23, pp. 10871-1–10871-5, 2004.
[9] G. Lozano *et al.*, "Plasmonics for solid-state lighting: Enhanced excitation and directional emission of highly efficient light sources," *Light Sci. Appl.*, vol. 2, no. 5, p. e66, 2013.
[10] G. Lozano, S. R. K. Rodriguez, M. A. Verschuuren, and J. G. Rivas, "Metallic nanostructures for efficient LED lighting," *Light Sci. Appl.*, vol. 5, no. 6, p. e16080, 2016.
[11] P. Törmä and W. L. Barnes, "Strong coupling between surface plasmon polaritons and emitters: A review," *Rep. Prog. Phys.*, vol. 78, no. 1, 2014, Art. no. 013901.
[12] A. Vaskin, R. Kolkowski, A. F. Koenderink, and I. Staude, "Light-emitting metasurfaces," *Nanophotonics*, vol. 8, no. 7, pp. 1151–1198, 2019.
[13] F. Capolino, Ed., *Theory and Phenomena of Metamaterials*. Boca Raton, FL, USA: CRC Press, 2017.
[14] I. Sersic, M. A. van de Haar, F. B. Arango, and A. F. Koenderink, "Ubiquity of optical activity in planar metamaterial scatterers," *Phys. Rev. Lett.*, vol. 108, May 2012, Art. no. 223903.
[15] R. Alaee, M. Albooyeh, A. Rahimzadegan, M. S. Mirmoosa, Y. S. Kivshar, and C. Rockstuhl, "All-dielectric reciprocal bianisotropic nanoparticles," *Phys. Rev. B, Condens. Matter*, vol. 92, Dec. 2015, Art. no. 245130.
[16] I. Fernandez-Corbaton, M. Fruhnert, and C. Rockstuhl, "Objects of maximum electromagnetic chirality," *Phys. Rev. X*, vol. 6, no. 3, 2016, Art. no. 031013.
[17] M. Kerker, D.-S. Wang, and C. L. Giles, "Electromagnetic scattering by magnetic spheres," *J. Opt. Soc. Amer.*, vol. 73, no. 6, pp. 765–767, Jun. 1983.
[18] A. Alù and N. Engheta, "How does zero forward-scattering in magnetodielectric nanoparticles comply with the optical theorem?" *J. Nanophoton.*, vol. 4, no. 1, 2010, Art. no. 041590.
[19] B. Rolly, B. Stout, and N. Bonod, "Boosting the directivity of optical antennas with magnetic and electric dipolar resonant particles," *Opt. Express*, vol. 20, no. 18, pp. 20376–20386, 2012.
[20] C. Pfeiffer and A. Grbic, "Metamaterial huygens' surfaces: Tailoring wave fronts with reflectionless sheets," *Phys. Rev. Lett.*, vol. 110, no. 19, 2013, Art. no. 197401.
[21] K. E. Chong *et al.*, "Efficient polarization-insensitive complex wavefront control using huygens' metasurfaces based on dielectric resonant meta-atoms," *ACS Photon.*, vol. 3, no. 4, pp. 514–519, 2016.
[22] M. F. Picardi, A. V. Zayats, and F. J. Rodríguez-Fortuño, "Janus and huygens dipoles: Near-field directionality beyond spin-momentum locking," *Phys. Rev. Lett.*, vol. 120, no. 11, 2018, Art. no. 117402.
[23] L. Wang, R.-Y. Zhang, M. Xiao, D. Han, C. T. Chan, and W. Wen, "The existence of topological edge states in honeycomb plasmonic lattices," *New J. Phys.*, vol. 18, Oct. 2016, Art. no. 103029.
[24] P. Qiu *et al.*, "Topologically protected edge states in graphene plasmonic crystals," *Opt. Express*, vol. 25, no. 19, pp. 22587–22594, 2017.
[25] C.-R. Mann, T. J. Sturges, G. Weick, W. L. Barnes, and E. Mariani, "Manipulating type-I and type-II dirac polaritons in cavity-embedded honeycomb metasurfaces," *Nature Commun.*, vol. 9, no. 1, 2018, Art. no. 2194.
[26] M. Honari-Latifpour and L. Yousefi, "Topological plasmonic edge states in a planar array of metallic nanoparticles," *Nanophotonics*, vol. 8, no. 5, pp. 799–806, 2019.
[27] W. Zhou, Y. Hua, M. D. Huntington, and T. W. Odom, "Delocalized lattice plasmon resonances show dispersive quality factors," *J. Phys. Chem. Lett.*, vol. 3, no. 10, pp. 1381–1385, 2012.
[28] D. Wang *et al.*, "Band-edge engineering for controlled multi-modal nanolasing in plasmonic superlattices," *Nature Nanotechnol.*, vol. 12, pp. 889–894, Sep. 2017.
[29] H. Zhou *et al.*, "Observation of bulk Fermi arc and polarization half charge from paired exceptional points," *Science*, vol. 359, pp. 1009–1012, Mar. 2018.
[30] H. Shen, B. Zhen, and L. Fu, "Topological band theory for non-Hermitian Hamiltonians," *Phys. Rev. Lett.*, vol. 120, no. 14, 2018, Art. no. 146402.
[31] M. V. Berry and D. H. J. O'Dell, "Diffraction by volume gratings with imaginary potentials," *J. Phys. A, Math. Gen.*, vol. 31, no. 8, p. 2093, 1998.
[32] A. Cerjan, A. Raman, and S. Fan, "Exceptional contours and band structure design in parity-time symmetric photonic crystals," *Phys. Rev. Lett.*, vol. 116, no. 20, 2016, Art. no. 203902.
[33] H. Zhou, J. Y. Lee, S. Liu, and B. Zhen, "Exceptional surfaces in PT-symmetric non-Hermitian photonic systems," *Optica*, vol. 6, no. 2, pp. 190–193, 2019.
[34] M. V. Berry, "Physics of nonhermitian degeneracies," *Czechoslovak J. Phys.*, vol. 54, no. 10, pp. 1039–1047, 2004.
[35] A. Pick *et al.*, "General theory of spontaneous emission near exceptional points," *Opt. Express*, vol. 25, no. 11, pp. 12325–12348, 2017.
[36] B. Zhen *et al.*, "Spawning rings of exceptional points out of Dirac cones," *Nature*, vol. 525, pp. 354–358, Sep. 2015.
[37] M. V. Berry, "Optical polarization evolution near a non-Hermitian degeneracy," *J. Opt.*, vol. 13, no. 11, 2011, Art. no. 115701.
[38] N. Parappurath, F. Alpeggiani, L. Kuipers, and E. Verhagen, "Direct observation of topological edge states in silicon photonic crystals: Spin, dispersion, and chiral routing," 2018,

arXiv:1811.10739. [Online]. Available: https://arxiv.org/abs/1811.10739

[39] M. Lawrence *et al.*, "Manifestation of PT symmetry breaking in polarization space with terahertz metasurfaces," *Phys. Rev. Lett.*, vol. 113, no. 9, 2014, Art. no. 093901.

[40] P. P. Ewald, "Die Berechnung optischer und elektrostatischer Gitterpotentiale," *Ann. Phys.*, vol. 369, no. 3, pp. 253–287, 1921.

[41] K. E. Jordan, G. R. Richter, and P. Sheng, "An efficient numerical evaluation of the Green's function for the Helmholtz operator on periodic structures," *J. Comput. Phys.*, vol. 63, no. 1, pp. 222–235, 1986.

[42] F. J. G. de Abajo, "*Colloquium*: Light scattering by particle and hole arrays," *Rev. Mod. Phys.*, vol. 79, no. 4, p. 1267, 2007.

[43] B. Gallinet, A. M. Kern, and O. J. F. Martin, "Accurate and versatile modeling of electromagnetic scattering on periodic nanostructures with a surface integral approach," *J. Opt. Soc. Amer. A, Opt. Image Sci.*, vol. 27, no. 10, pp. 2261–2271, Oct. 2010.

[44] A. Kwadrin and A. F. Koenderink, "Diffractive stacks of metamaterial lattices with a complex unit cell: Self-consistent long-range bianisotropic interactions in experiment and theory," *Phys. Rev. B, Condens. Matter*, vol. 89, no. 4, 2014, Art. no. 045120.

[45] P. Lunnemann and A. F. Koenderink, "Dispersion of guided modes in two-dimensional split ring lattices," *Phys. Rev. B, Condens. Matter*, vol. 90, no. 24, 2014, Art. no. 245416.

[46] Y. Mazor and B. Z. Steinberg, "Metaweaves: Sector-way nonreciprocal metasurfaces," *Phys. Rev. Lett.*, vol. 112, Apr. 2014, Art. no. 153901.

[47] S. Baur, S. Sanders, and A. Manjavacas, "Hybridization of lattice resonances," *ACS Nano*, vol. 12, no. 2, pp. 1618–1629, 2018.

[48] E. M. Purcell and C. R. Pennypacker, "Scattering and absorption of light by nonspherical dielectric grains," *Astrophys. J.*, vol. 186, pp. 705–714, Dec. 1973.

[49] B. T. Draine and P. J. Flatau, "Discrete-dipole approximation for scattering calculations," *J. Opt. Soc. Amer. A, Opt. Image Sci.*, vol. 11, no. 4, pp. 1491–1499, 1994.

[50] A. Lagendijk and B. A. van Tiggelen, "Resonant multiple scattering of light," *Phys. Rep.*, vol. 270, no. 3, pp. 143–215, 1996.

[51] P. de Vries, D. V. van Coevorden, and A. Lagendijk, "Point scatterers for classical waves," *Rev. Mod. Phys.*, vol. 70, no. 2, pp. 447–466, Apr. 1998.

[52] I. V. Lindell, A. H. Sihvola, S. A. Tretyakov, and A. J. Viitanen, *Electromagnetic Waves in Chiral and Bi-Isotropic Media*. Norwood, MA, USA: Artech House, 1994.

[53] P. A. Belov, S. I. Maslovski, K. R. Simovski, and S. A. Tretyakov, "A condition imposed on the electromagnetic polarizability of a bianisotropic lossless scatterer," *Tech. Phys. Lett.*, vol. 29, no. 9, pp. 718–720, 2003.

[54] I. Sersic, C. Tuambilangana, T. Kampfrath, and A. F. Koenderink, "Magnetoelectric point scattering theory for metamaterial scatterers," *Phys. Rev. B, Condens. Matter*, vol. 83, no. 24, Art. no. 245102, 2011.

[55] R. Alaee *et al.*, "Magnetoelectric coupling in nonidentical plasmonic nanoparticles: Theory and applications," *Phys. Rev. B, Condens. Matter*, vol. 91, Mar. 2015, Art. no. 115119.

[56] S. S. Kruk *et al.*, "Spin-polarized photon emission by resonant multipolar nanoantennas," *ACS Photon.*, vol. 1, no. 11, pp. 1218–1223, 2014.

[57] L. D. Landau and E. M. Lifshitz, *Electrodynamics of Continuous Media*. Oxford, U.K.: Pergamon, 1960.

[58] A. N. Serdyukov, I. V. Semchenko, S. A. Tretyakov, and A. Sihvola, *Electromagnetics of Bi-Anisotropic Materials: Theory and Applications*. Amsterdam, The Netherlands: Gordon and Breach, 2001.

[59] J. E. Sipe and J. van Kranendonk, "Macroscopic electromagnetic theory of resonant dielectrics," *Phys. Rev. A, Gen. Phys.*, vol. 9, no. 5, p. 1806, 1974.

[60] M. Kerker, "Resonances in electromagnetic scattering by objects with negative absorption," *Appl. Opt.*, vol. 18, no. 8, pp. 1180–1189, Apr. 1979.

[61] C. F. Bohren and D. R. Huffman, *Absorption and Scattering of Light by Small Particles*. Hoboken, NJ, USA: Wiley, 1998.

[62] W. L. Barnes, "Particle plasmons: Why shape matters," *Amer. J. Phys.*, vol. 84, no. 8, pp. 593–601, 2016.

[63] X. Fan, W. Zheng, and D. J. Singh, "Light scattering and surface plasmons on small spherical particles," *Light Sci. Appl.*, vol. 3, no. 6, p. e179, 2014.

[64] A. Alù and N. Engheta, "Achieving transparency with plasmonic and metamaterial coatings," *Phys. Rev. E, Stat. Phys. Plasmas Fluids Relat. Interdiscip. Top.*, vol. 72, no. 1, Jul. 2005, Art. no. 016623.

[65] M. Arnold, M. Blaber, and M. Ford, "Local plasmon resonances of metal-in-metal core-shells," *Opt. Express*, vol. 22, no. 3, pp. 3186–3198, 2014.

[66] P. B. Johnson and R.-W. Christy, "Optical constants of the noble metals," *Phys. Rev. B, Condens. Matter*, vol. 6, no. 12, p. 4370, 1972.

[67] A. D. Rakić, A. B. Djurišić, J. M. Elazar, and M. L. Majewski, "Optical properties of metallic films for vertical-cavity optoelectronic devices," *Appl. Opt.*, vol. 37, no. 22, pp. 5271–5283, 1998.

[68] A. Manjavacas, "Anisotropic optical response of nanostructures with balanced gain and loss," *ACS Photon.*, vol. 3, no. 7, pp. 1301–1307, 2016.

[69] F. Salin and J. Squier, "Gain guiding in solid-state lasers," *Opt. Lett.*, vol. 17, no. 19, pp. 1352–1354, 1992.

[70] C. Z. Ning, "Semiconductor nanolasers," *Phys. Status Solidi B*, vol. 247, no. 4, pp. 774–788, Apr. 2010.

[71] G. Somasundaram and A. Ramalingam, "Gain studies of Rhodamine 6G dye doped polymer laser," *J. Photochem. Photobiol. A, Chem.*, vol. 125, nos. 1–3, pp. 93–98, 1999.

[72] S. Y. Lam and M. J. Damzen, "Characterisation of solid-state dyes and their use as tunable laser amplifiers," *Appl. Phys. B*, vol. 77, nos. 6–7, pp. 577–584, 2003.

[73] H. Kim, N. Schulte, G. Zhou, K. Müllen, and F. Laquai, "A high gain and high charge carrier mobility indenofluorene-phenanthrene copolymer for light amplification and organic lasing," *Adv. Mater.*, vol. 23, no. 7, pp. 894–897, 2011.

[74] M. Amyot-Bourgeois, E. K. Keshmarzi, C. Hahn, R. N. Tait, and P. Berini, "Gain optimization, bleaching, and e-beam structuring of IR-140 doped PMMA and integration with plasmonic waveguides," *Opt. Mater. Express*, vol. 7, no. 11, pp. 3963–3978, 2017.

[75] D. Geskus, S. Aravazhi, S. M. García-Blanco, and M. Pollnau, "Giant optical gain in a rare-earth-ion-doped microstructure," *Adv. Mater.*, vol. 24, no. 10, pp. OP19–OP22, 2012.

[76] C. H. Lin *et al.*, "Core/alloyed-shell quantum dot robust solid films with high optical gains," *ACS Photon.*, vol. 3, no. 4, pp. 647–658, 2016.

[77] J. Leuthold, M. Mayer, J. Eckner, G. Guekos, and H. Melchior, "Material gain of bulk 1.55 μm InGaAsP/InP semiconductor optical amplifiers approximated by a polynomial model," *J. Appl. Phys.*, vol. 87, no. 1, pp. 618–620, 2000.

[78] B. R. Sutherland *et al.*, "Perovskite thin films via atomic layer deposition," *Adv. Mater.*, vol. 27, no. 1, pp. 53–58, 2015.

[79] B. Guzelturk, M. Pelton, M. Olutas, and H. V. Demir, "Giant modal gain coefficients in colloidal II–VI nanoplatelets," *Nano Lett.*, vol. 19, no. 1, pp. 277–282, 2019.

[80] R. Dingle, K. L. Shaklee, R. F. Leheny, and R. B. Zetterstrom, "Stimulated emission and laser action in gallium nitride," *Appl. Phys. Lett.*, vol. 19, no. 1, pp. 5–7, 1971.

[81] N. Kirstaedter *et al.*, "Gain and differential gain of single layer InAs/GaAs quantum dot injection lasers," *Appl. Phys. Lett.*, vol. 69, pp. 1226–1228, Aug. 1996.

[82] V. N. Pustovit, A. M. Urbas, A. V. Chipouline, and T. V. Shahbazyan, "Coulomb and quenching effects in small nanoparticle-based spasers," *Phys. Rev. B, Condens. Matter*, vol. 93, no. 16, 2016, Art. no. 165432.

[83] M. I. Stockman, "The spaser as a nanoscale quantum generator and ultrafast amplifier," *J. Opt.*, vol. 12, no. 2, 2010, Art. no. 024004.

[84] R. Berera, R. van Grondelle, and J. T. M. Kennis, "Ultrafast transient absorption spectroscopy: Principles and application to photosynthetic systems," *Photosynthesis Res*, vol. 101, nos. 2–3, pp. 105–118, 2009.

[85] A. Poddubny, A. Miroshnichenko, A. Slobozhanyuk, and Y. Kivshar, "Topological majorana states in ZigZag chains of plasmonic nanoparticles," *ACS Photon.*, vol. 1, no. 2, pp. 101–105, 2014.

[86] N. Yu and F. Capasso, "Flat optics with designer metasurfaces," *Nature Mater.*, vol. 13, pp. 139–150, Jan. 2014.

[87] M. C. Rechtsman *et al.*, "Photonic floquet topological insulators," *Nature*, vol. 496, pp. 196–200, Apr. 2013.

[88] A. Szameit, M. C. Rechtsman, O. Bahat-Treidel, and M. Segev, "PT-symmetry in honeycomb photonic lattices," *Phys. Rev. A, Gen. Phys.*, vol. 84, Aug. 2011, Art. no. 021806.

[89] H. Ramezani, T. Kottos, V. Kovanis, and D. N. Christodoulides, "Exceptional-point dynamics in photonic honeycomb lattices with PT symmetry," *Phys. Rev. A, Gen. Phys.*, vol. 85, no. 1, 2012, Art. no. 013818.

[90] M. Turduev *et al.*, "Two-dimensional complex parity-time-symmetric photonic structures," *Phys. Rev. A, Gen. Phys.*, vol. 91, no. 2, 2015, Art. no. 023825.

[91] C. Yuce and Z. Oztas, "PT symmetry protected non-Hermitian topological systems," *Sci. Rep.*, vol. 8, no. 1, 2018, Art. no. 17416.

[92] X. Ni, D. Smirnova, A. Poddubny, D. Leykam, Y. Chong, and A. B. Khanikaev, "PT phase transitions of edge states at PT symmetric interfaces in non-Hermitian topological insulators," *Phys. Rev. B, Condens. Matter*, vol. 98, no. 16, 2018, Art. no. 165129.

[93] M. Kremer, T. Biesenthal, L. J. Maczewsky, M. Heinrich, R. Thomale, and A. Szameit, "Demonstration of a two-dimensional PT-symmetric crystal: Bulk dynamics, topology, and edge states," *Nature Commun.*, vol. 10, p. 435, Aug. 2019.

[94] R. Guo, M. Nečada, T. K. Hakala, A. I. Väkeväinen, and P. Törmä, "Lasing at K points of a honeycomb plasmonic lattice," *Phys. Rev. Lett.*, vol. 122, no. 1, 2019, Art. no. 013901.

[95] M. V. Berry and M. Wilkinson, "Diabolical points in the spectra of triangles," *Proc. Roy. Soc. London A, Math. Phys. Sci.*, vol. 392, no. 1802, pp. 15–43, 1984.

[96] G. Weick, C. Woollacott, W. L. Barnes, O. Hess, and E. Mariani, "Dirac-like plasmons in honeycomb lattices of metallic nanoparticles," *Phys. Rev. Lett.*, vol. 110, no. 10, 2013, Art. no. 106801.

[97] P. Lunnemann, I. Sersic, and A. F. Koenderink, "Optical properties of two-dimensional magnetoelectric point scattering lattices," *Phys. Rev. B, Condens. Matter*, vol. 88, no. 24, 2013, Art. no. 245109.

[98] A. Christ, S. G. Tikhodeev, N. A. Gippius, J. Kuhl, and H. Giessen, "Waveguide-plasmon polaritons: Strong coupling of photonic and electronic resonances in a metallic photonic crystal slab," *Phys. Rev. Lett.*, vol. 91, no. 18, p. 183901, Oct. 2003.

[99] G. Vecchi, V. Giannini, and J. G. Rivas, "Shaping the fluorescent emission by lattice resonances in plasmonic crystals of nanoantennas," *Phys. Rev. Lett.*, vol. 102, no. 14, 2009, Art. no. 146807.

[100] S. R. K. Rodriguez, S. Murai, M. A. Verschuuren, and J. G. Rivas, "Light-emitting waveguide-plasmon polaritons," *Phys. Rev. Lett.*, vol. 109, no. 16, 2012, Art. no. 166803.

[101] W. Zhou *et al.*, "Lasing action in strongly coupled plasmonic nanocavity arrays," *Nature Nanotechnol.*, vol. 8, no. 7, pp. 506–511, 2013.

[102] A. I. Väkeväinen *et al.*, "Plasmonic surface lattice resonances at the strong coupling regime," *Nano. Lett.*, vol. 14, no. 4, pp. 1721–1727, 2014.
[103] M. Ramezani *et al.*, "Plasmon-exciton-polariton lasing," *Optica*, vol. 4, no. 1, pp. 31–37, 2017.
[104] T. K. Hakala *et al.*, "Lasing in dark and bright modes of a finite-sized plasmonic lattice," *Nature Commun.*, vol. 8, Jan. 2017, Art. no. 13687.
[105] X. M. Bendaña, G. Lozano, G. Pirruccio, J. G. Rivas, and F. J. García de Abajo, "Excitation of confined modes on particle arrays," *Opt. Express*, vol. 21, no. 5, pp. 5636–5642, 2013.
[106] D. Wang, A. Yang, A. J. Hryn, G. C. Schatz, and T. W. Odom, "Superlattice plasmons in hierarchical Au nanoparticle arrays," *ACS Photon.*, vol. 2, no. 12, pp. 1789–1794, 2015.
[107] E. Devaux, T. W. Ebbesen, J.-C. Weeber, and A. Dereux, "Launching and decoupling surface plasmons via micro-gratings," *Appl. Phys. Lett.*, vol. 83, pp. 4936–4938, Dec. 2003.
[108] R. M. Bakker *et al.*, "Near-field excitation of nanoantenna resonance," *Opt. Express*, vol. 15, no. 21, pp. 13682–13688, 2007.
[109] A. L. Koh *et al.*, "Electron energy-loss spectroscopy (EELS) of surface plasmons in single silver nanoparticles and dimers: Influence of beam damage and mapping of dark modes," *ACS Nano*, vol. 3, no. 10, pp. 3015–3022, 2009.
[110] T. Coenen, E. J. R. Vesseur, A. Polman, and A. F. Koenderink, "Directional emission from plasmonic Yagi–Uda antennas probed by angle-resolved cathodoluminescence spectroscopy," *Nano Lett.*, vol. 11, no. 9, pp. 3779–3784, 2011.
[111] A. Slobozhanyuk *et al.*, "Near-field imaging of spin-locked edge states in all-dielectric topological metasurfaces," *Appl. Phys. Lett.*, vol. 114, no. 3, 2019, Art. no. 031103.
[112] J. Zak, "Band representations and symmetry types of bands in solids," *Phys. Rev. B, Condens. Matter*, vol. 23, no. 6, p. 2824, 1981.
[113] C. Kittel, *Introduction to Solid State Physics*, vol. 8. New York, NY, USA: Wiley, 1996.
[114] N. W. Ashcroft and N. D. Mermin, *Solid State Physics*. Boston, MA, USA: Cengage Learning, 2011.
[115] C. E. Rüter, K. G. Makris, R. El-Ganainy, D. N. Christodoulides, M. Segev, and D. Kip, "Observation of parity–time symmetry in optics," *Nature Phys.*, vol. 6, no. 3, pp. 192–195, 2010.
[116] M. V. Berry, "Quantal phase factors accompanying adiabatic changes," *Proc. Roy. Soc. London*, vol. 392, no. 1802, pp. 45–57, 1984.
[117] S. R. Pocock, X. Xiao, P. A. Huidobro, and V. Giannini, "Topological plasmonic chain with retardation and radiative effects," *ACS Photon.*, vol. 5, no. 6, pp. 2271–2279, 2018.
[118] H. Kwon, D. Sounas, A. Cordaro, A. Polman, and A. Alù, "Nonlocal metasurfaces for optical signal processing," *Phys. Rev. Lett.*, vol. 121, no. 17, 2018, Art. no. 173004.
[119] M. Greenberg and M. Orenstein, "Irreversible coupling by use of dissipative optics," *Opt. Lett.*, vol. 29, no. 5, pp. 451–453, 2004.
[120] A. Krasnok, M. Tymchenko, and A. Alù, "Nonlinear metasurfaces: A paradigm shift in nonlinear optics," *Mater. Today*, vol. 21, no. 1, pp. 8–21, 2017.
[121] T. T. Koutserimpas, A. Alù, and R. Fleury, "Parametric amplification and bidirectional invisibility in PT-symmetric time-Floquet systems," *Phys. Rev. A, Gen. Phys.*, vol. 97, no. 1, 2018, Art. no. 013839.
[122] Y. T. Chen, Y. Zhang, and A. F. Koenderink, "General point dipole theory for periodic metasurfaces: Magnetoelectric scattering lattices coupled to planar photonic structures," *Opt. Express*, vol. 25, no. 18, pp. 21358–21378, 2017.
[123] K. Guo and A. F. Koenderink, "Spatial intensity distribution in plasmonic particle array lasers," *Phys. Rev. Appl.*, vol. 11, no. 2, 2019, Art. no. 024025.
[124] K. Guo, S. Kasture, and A. F. Koenderink, "Plasmon antenna array 'patchwork' lasers—Towards low etendue, speckle free light sources," *OSA Continuum*, vol. 2, no. 6, pp. 1982–1997, 2019.

ABOUT THE AUTHORS

AQ:4

Radoslaw Kolkowski received the Ph.D. degree jointly from the Wroclaw University of Science and Technology, Wroclaw, Poland (chemistry) and ENS Paris-Saclay, Cachan, France (physics), in 2016. His dissertation was on nonlinear optical phenomena in plasmonic nanostructures.

From 2016 to 2018, he was a Postdoctoral Fellow with the Physics Department, Technion—Israel Institute of Technology, Haifa, Israel. Since 2018, he has been a Postdoctoral Researcher with AMOLF, Amsterdam, The Netherlands. His current research interests include optical properties of periodic and resonant nanostructures with anisotropy, chirality, amplification, and nonreciprocal and nonlinear effects.

A. Femius Koenderink received the Ph.D. degree in physics from the University of Amsterdam, Amsterdam, The Netherlands, in 2003, with a focus on transport and emission of light in 3-D photonic crystals.

He was a Postdoctoral Researcher with the Swiss Federal Institute of Technology (ETH Zürich), Zürich, Switzerland. He joined the National Research Institute AMOLF, Amsterdam, where he started a group in 2008 to work on the physics of scattering and fluorescence of plasmonic antennas and metamaterial scatterers. Since 2012, he has been a Full Professor with the Institute of Physics, University of Amsterdam. Since 2016, he has been the Head of the Center for Nanophotonics, AMOLF. His current research interests include emission control and lasing in plasmon nanocavity array systems, light–matter interaction in resonators with plasmonic confinement yet microcavity quality factor, and the development of real-space and Fourier space microscopy techniques to quantify the physics of single nanostructures and single emitters.